Thermal Conduction and Electron Heating in Solar Coronal Mass Ejections

A Thesis

submitted to
Indian Institute of Science Education and Research, Pune
in partial fulfillment of the requirements for the
BS-MS Dual Degree Programme

by

Saikat Majumder

Indian Institute of Science Education and Research, Pune
Dr. Homi Bhabha Road,
Pashan, Pune – 411008, INDIA.

April, 2023

Supervisor: **Prof. Prasad Subramanian**

© **Saikat Majumder** 2023

All rights reserved

Certificate

This is to certify that this dissertation entitled **Thermal Conduction and Electron Heating in Solar Coronal Mass Ejections** towards the partial fulfilment of the BS-MS Dual Degree Programme at the Indian Institute of Science Education and Research, Pune represents the study/work carried out by **Saikat Majumder** at Indian Institute of Science Education and Research under the supervision of **Prof. Prasad Subramanian**, Professor, Department of Physics, during the academic year 2022-2023.

Prof. Prasad Subramanian

Committee:

Prof. Prasad Subramanian

Dr. Seema Sharma

This thesis is dedicated to –

Professor Prasad Subramanian

&

Debesh Bhattacharjee

Declaration

I hereby declare that the matter embodied in the report entitled **Thermal Conduction and Electron Heating in Solar Coronal Mass Ejections** are the results of the work carried out by me at the Department of Physics, Indian Institute of Science Education and Research, Pune, under the supervision of **Prof. Prasad Subramanian** and the same has not been submitted elsewhere for any other degree.

Saikat Majumder.

Saikat Majumder

Acknowledgments

As I come to the end of my five-year journey as a BS-MS student at IISER Pune, I reflect on the fleeting nature of time. Time has passed far too quickly for me to relish the feelings I experienced throughout. And I often wonder how one single decision can alter the course of your life so drastically that it becomes incomprehensible to imagine how things might have been different had you made another choice. I have always been fascinated by Astronomy and Astrophysics, and the pursuit of this childhood curiosity led me to IISER. My decision to join IISER Pune has allowed me to gain profound experiences, and now I cannot help but think about the people who have made these five years of my life worth living.

Firstly, I express my sincerest gratitude to my supervisor, Professor Prasad Subramanian, for his unwavering support and invaluable guidance throughout my time under his supervision. He picked me up from a dire state of confusion and hopelessness and allowed me to reinvent myself. He probably had no idea of my circumstances before I joined his group, but due to his trust in my abilities, I regained my confidence and started to do better. His exceptional teaching skills were the primary driver for my interest in plasma astrophysics. His profound knowledge of the subject and his insights on how to tackle any problem were instrumental in shaping my ideas and refining the direction of my work. I thoroughly enjoyed all the discussions on science and music we had over the last year. This thesis is a result of his constant encouragement and motivation. Saying “thank you” cannot possibly justify the role he played in making this thesis a reality.

I am immensely grateful to my thesis advisory committee (TAC) expert member, Dr. Seema Sharma, for providing her valuable time and effort in reviewing my work and offering constructive suggestions. Her insightful feedback helped to enrich the quality of my research. Apart from guiding me as a TAC member, she had also previously mentored me during my early undergrad years, which helped me enormously during those trying times. I would also like to express my appreciation to IISER Pune, all the faculty members, administration, library, security, dining and housekeeping staff who have made our lives easier.

I am deeply indebted to Debesh Da for always being there for me as my groupmate, elder brother and confidante. Due to his cheerful attitude towards research and nature, I learned to appreciate both my work and my life. As he has rightfully mentioned, I had the privilege of becoming his (and Chandra Di's) little brother in every possible way. I will forever remember the times I spent with him – from our discussions on physics, books, World War II, art, music, anime, food and life to hosting events and travelling to several conferences together. His ideas have significantly contributed to the growth of my personal self and this research project. I also thank previous members of the Plasma Astrophysics group at IISER Pune, namely, Dr. Nishtha Sachdeva for providing me with the data on which my work is based, Niranjana, whose previous work with Prof. Prasad gave me the background of my thesis and Mayur for our exciting discussions and dinner parties.

A special mention goes to Soumi for the role she played in keeping me hopeful throughout the last year. I have cherished every single moment we shared. Her constant presence, despite the distance, made it easy for me to deal with the challenges I faced. Thank you for putting up with me and always staying by my side. On the same note, I thank Tammy for being the most loving sister one could ask for.

I have had the fortune of meeting an amazing group of people I can proudly call my support system. Archi di, Arijit da, Supritha, Hari, Debjyoti da and Ranita di, thank you so much for making me a part of your lives. This last year, I have fulfilled my dream of organizing and performing in several cultural extravaganzas at IISER. The people who have made it possible range from my supportive seniors – Ayan da, Ritwick da, Sagnik da, Korak da, Indra da, Joy da, Ratheejit da, Shruti di, Avisikta di, Megha di, Somashree di, Ajit da, Anusua di, Souvik da, Mridul da, Sayan da, Sudipto da, Souradeep da, Vineet and others, to my outstanding juniors – Abhradeep, Vishak, Shayandeep, Shalini, Barish, Manjima, Gaurav, Ryth, Deepjit, Rajat and many more. I have pampered them again and again, yet they have been on my side.

And how can I forget my extraordinary friends and batchmates who have been on the same journey as me. Starting with my the friends I first made at IISER – Shikhar, Devarsh, Sanskar, Sarang, Nitish, Uday, Komal, Raju, Siddharth, Animesh and more. From having hostel-cooked food together, solving assignments just before submission deadline, to going on sudden trips, you guys have made my college life more fun than I expected. Special thanks to Lubdhak, Prantik, Kunal, Dipayan, Deepesh, Sahil, Saket, Bishal and others. I will forever cherish our memories of musical jamming (courtesy of Lubdhak, who started it all), adda, partying, and travelling.

I owe an immeasurable debt of gratitude to my parents – Maa and Baba, my elder brother Biki, Sonai, Dida and the rest of my family for their unending love and encouragement throughout my life. Without their sacrifices and endless support, I would not be where I am today. They have always believed in my abilities and helped me achieve my goal. Their contribution to my success is unfathomable, and mere words cannot express my appreciation for everything they have done for me.

Lastly, I am thankful to everyone who has influenced my life in some way and challenged, inspired, and encouraged me along the way. Their kindness, generosity, and wisdom have made these five years of my life worthwhile, and I am honoured to have had the opportunity to spend my time with you all. My dreams and aspirations have been made possible due to everyone's role in making them a reality, and I heartily thank you all from the bottom of my heart.

(*This illustration of the Main Building of IISER Pune is taken from the IISER Pune Institute Profile Brochure 2020.*)

Abstract

Massive eruptions of plasma and magnetic fields from the solar corona, called Coronal Mass Ejections (CMEs), are significant drivers of space weather phenomena and can cause extreme geomagnetic storms if Earth-directed. Therefore, reliable estimates of CME arrival times and a thorough understanding of CME dynamics are crucial for space weather forecasting. If CMEs were to expand adiabatically, their temperature at 1 AU would be about a few degrees of kelvin. However, the observed proton temperatures are as high as $\approx 10^5$ K. This discrepancy suggests that either there is sufficient thermal conduction from the Sun to the CME interior or substantial plasma heating happening inside the CMEs. We examine the first possibility in this work by considering electron thermal conduction. We have computed the CME propagation velocities and electron thermal conduction front velocities for a collection of 38 Earth-directed CMEs using semi-empirical models, remote sensing images from SOHO/LASCO and STEREO/SECCHI coronagraphs, as well as in situ data from WIND spacecraft. The conduction velocities are estimated for purely Spitzer thermal conductivity and two different types of turbulence-modified anomalous thermal conductivities. Comparison between the CME propagation and conduction velocities shows that thermal conduction is much faster than CME propagation for Spitzer conductivity, while it is less fast for Kolmogorov turbulence-modified conductivity. The two speeds become comparable for conductivity modified by Kraichnan turbulence. These results are consistent across all 38 events. This seems to imply that thermal conduction is sufficient to explain the high electron temperature in the CME interior, and thus CME expansion can be modelled as nearly isothermal. However, thermal conduction cannot be an explanation for protons, since it is very inefficient. We have further calculated the heating rate of electron-proton equilibration and found that it is quite small. Our results, therefore, justify the need for invoking additional heating mechanisms (such as turbulent heating) for protons.

Contents

Abstract **xiii**

1 Introduction **5**

1.1 Coronal Mass Ejections 5

1.1.1 Properties 6

1.1.2 Origin 6

1.1.3 Observations and Morphology 6

1.2 Heating of CMEs 9

1.3 Effects on Space Weather 10

2 Motivation and Outline **11**

2.1 Why thermal conduction in CMEs? 11

2.2 Thesis Organization 13

3 Methodology **15**

3.1 Introduction to Magnetohydrodynamics (MHD) 15

3.1.1 The MHD Approximation 15

3.1.2 Ideal MHD 16

3.1.3 Resistive MHD 17

3.2 Electron Thermal Conduction inside CMEs using Spitzer Conductivity 18

3.3 Electron Thermal Conduction inside CMEs using non-Spitzer Conductivity 20

3.3.1 Calculation of Anomalous (non-Spitzer) Conductivity 22

3.4 CME Parameter Values from Solar Wind Model 23

4 Data and Analysis 25

4.1 CME Velocity using GCS fitted data 25

5 Results and Discussion 29

5.1 Timescale vs Distance Plots 29

5.1.1 Spitzer Timescale Profiles 30

5.1.2 Non-Spitzer Timescale Profiles 31

5.2 Velocity vs Distance Plots 33

5.2.1 Spitzer Case 35

5.2.2 Kraichnan Case 36

5.2.3 Kolmogorov Case 36

5.3 Proton Heating through Thermal Equilibration 38

6 Conclusions and Future Work 41

6.1 Electron Thermal Conduction 41

6.1.1 Spitzer Case 41

6.1.2 Anomalous or Non-Spitzer Case 41

6.2 Proton Heating Rates 42

6.3 Future Work 42

7 Appendix 45

7.1 Table of Physical Constants and Plasma Parameters 45

7.2 Timescale vs Distance Plots for the other CMEs 46

7.3 Velocity vs Distance Plots for the other CMEs 53

7.4 Proton Heating Rate vs Distance Plots for the other CMEs 60

Bibliography **66**

List of Tables

4.1 List of the 38 CMEs shortlisted by Sachdeva et al. (2017) [1] for the period of March 2010 to December 2013. Fast CMEs are designated by a superscript f. The 15 events indicated with an asterisk (*) coincide with the near-Earth counterparts of WIND events from Table A.1 of Bhattacharjee et al. (2022) [2]. 28

7.1 Numerical values of physical constants and plasma parameters used in this thesis. This table is made using Appendices A and D of *Physics of the Solar Corona* by Aschwanden (2005) [3]. 45

List of Figures

1.1 Three-part structure CMEs as seen by SOHO LASCO C2 on December 2, 2002 (Left) and LASCO C3 on February 2, 2002 (Right). Images are taken from `https://soho.nascom.nasa.gov/gallery/bestofsoho.html`. 7

1.2 (a) Cartoon showing ICME evolution with background solar wind. The LASCO Coronagraph image is superimposed with a flux rope fitting. (b) An ICME column expansion. Image taken from Dasso et al. (2012) [4]. 8

1.3 ICME Diagram with corresponding in situ properties. The left panel shows a classic ICME schematic (Zurbuchen and Richardson (2006) [5]). The right panel image is taken from Möstl et al. (2010) [6]. 9

4.1 Schematic diagram to represent the GCS model geometry in (a) face-on view and (b) edge-on view. This image is taken from Thernisien (2011) [7]. 26

5.1 Spitzer Timescales vs Distance Plots for CME2 and CME11 30

5.2 Non-Spitzer Timescales vs Distance Plots for CME2 31

5.3 Non-Spitzer Timescales vs Distance Plots for CME11 32

5.4 Velocity Profiles for CME2 and CME11 34

5.5 A cartoon of ICME showing the direction of electron propagation and heat flux. This image is modified from Wang et al. (2010) [8]. 35

5.6 A comparison between three different conduction scenarios. 37

5.7 Heating Rate vs Distance Plots for CME2 and CME11 39

7.1 Timescale Profiles for CME1 & CME3 46

7.2 Timescale Profiles for CME4 & CME5 47

7.3 Timescale Profiles for CME6 & CME17 48

7.4 Timescale Profiles for CME26 & CME27 49

7.5 Timescale Profiles for CME29 & CME30 50

7.6 Timescale Profiles for CME31 & CME33 51

7.7 Timescale Profiles for CME34 52

7.8 Velocity Profiles for CME1 & CME3 53

7.9 Velocity Profiles for CME4 & CME5 54

7.10 Velocity Profiles for CME6 & CME17 55

7.11 Velocity Profiles for CME26 & CME27 56

7.12 Velocity Profiles for CME29 & CME30 57

7.13 Velocity Profiles for CME31 & CME33 58

7.14 Velocity Profiles for CME34 59

7.15 Heating Rate Profiles for CME1 & CME3 60

7.16 Heating Rate Profiles for CME4 & CME5 61

7.17 Heating Rate Profiles for CME6 & CME17 62

7.18 Heating Rate Profiles for CME26 & CME27 63

7.19 Heating Rate Profiles for CME29 & CME30 64

7.20 Heating Rate Profiles for CME31 & CME33 65

7.21 Heating Rate Profiles for CME34 66

Chapter 1

Introduction

1.1 Coronal Mass Ejections

Coronal Mass Ejections (CMEs) are huge, intense outbursts of plasma and magnetic fields from the solar corona into interplanetary space. These are among the most energetic explosive events in the solar system and a major cause of adverse space weather conditions in the near-Earth space environment. These occurrences are connected with large-scale disruptions in the solar corona and can generate shocks and magnetic disturbances that travel through the solar wind and interact with the Earth's magnetic field. Studying the dynamics and energetics of CMEs is crucial for accurate space weather forecasting and mitigation efforts.

An understanding of the energy dissipation mechanisms inside CMEs is vital in building reliable models for their propagation. CMEs propagating through the heliosphere are termed as Interplanetary CMEs (ICMEs). Earth-directed ICMEs often cause geomagnetic storms upon impact with the Earth's magnetic field. Technologies we often use on a daily basis can be severely affected by these storms. This has sparked substantial research into how CMEs are formed in the solar corona, how they propagate across the heliosphere and how much energy is spent in expanding and heating a propagating ICME. Answers to these critical questions will have a significant impact on our knowledge of CME dynamics. We now briefly highlight some key characteristics of CMEs to get an overview of these solar eruptive phenomena.

1.1.1 Properties

Typical CMEs have masses in the range of $10^{14} - 10^{16}\,\mathrm{g}$, densities of about $10^{6} - 10^{7}\,\mathrm{cm}^{-3}$, and temperatures of $\approx 10^{6}\,\mathrm{K}$ near Sun (Gopalswamy and Kundu (1992) [9]). Their velocities can be about $10^{2} - 2 \times 10^{3}\,\mathrm{km\,s}^{-1}$ (Yurchyshyn et al. (2005) [10]) and kinetic energies are of the order $10^{29} - 10^{31}\,\mathrm{erg\,s}^{-1}$ (Vourlidas et al. (2010) [11]). The occurrence rate of CMEs tracks the 11-year solar activity cycle. The leading edge CME velocity is found to increase during solar maximum.

1.1.2 Origin

Magnetic fields of the solar corona rooted below the photosphere are continuously twisted and deformed due to the differential rotation of the Sun. This generates significant stress and strain in the field lines, causing magnetic reconnection which releases the stored energy in the form of a CME. This magnetic free energy can accelerate the CMEs to several hundred kilometres per second against the Sun's gravity and transport massive quantities of plasma and magnetic fields into the interplanetary medium. Various theoretical models of CME initiation are explained in Chen (2011) [12].

1.1.3 Observations and Morphology

Remote-sensing measurements

Typically, CMEs are visible in the solar corona as bright, elongated structures referred to as *transients* that can stretch many solar radii from the Sun's surface. CMEs are best observed with a white light coronagraph, which obscures the bright solar disk to image the much fainter corona. It creates an artificial solar eclipse by blocking off the Sun's primary disk. This draws the Sun's corona into clear focus. Figure 1.1 shows two CMEs observed from the Large Angle Spectrometric Coronagraph (LASCO) on board SOHO, having a three-part structure of a bright frontal loop (leading edge), followed by a darker cavity (embedded flux rope), and a bright core corresponding to a filament eruption (Illing and Hundhausen (1985) [13]). The central disk is the occulter which blocks the bright solar disk (represented by the white circle). However, not all CMEs possess this standard three-part morphology due to projection effects.

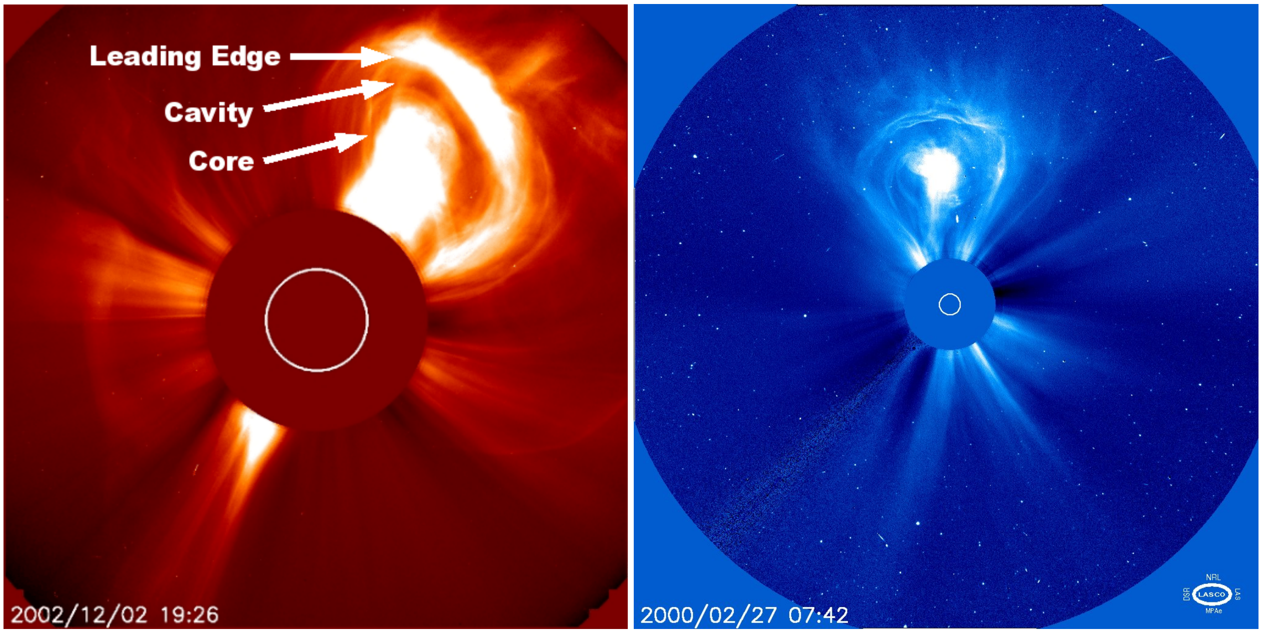

Figure 1.1: Three-part structure CMEs as seen by SOHO LASCO C2 on December 2, 2002 (Left) and LASCO C3 on February 2, 2002 (Right). Images are taken from https://soho.nascom.nasa.gov/gallery/bestofsoho.html.

CME Expansion

Interplanetary coronal mass ejections (ICMEs) are considered to have a magnetic flux rope structure, which is a flux tube with helical magnetic field lines that spiral around the axis of a curved cylindrical torus. ICMEs are observed to expand in both length and cross-section as they travel through the heliosphere. Models of ICME propagation assume that the legs of the magnetic flux rope structure are always connected to the Sun, i.e. the CME is anchored to the Sun as it extends into the interplanetary medium. The left panel in Figure 1.2 depicts a flux rope CME interacting with the ambient solar wind, and the right panel shows the subsequent expansion of the CME column as it evolves due to the decrease of the solar wind pressure with distance.

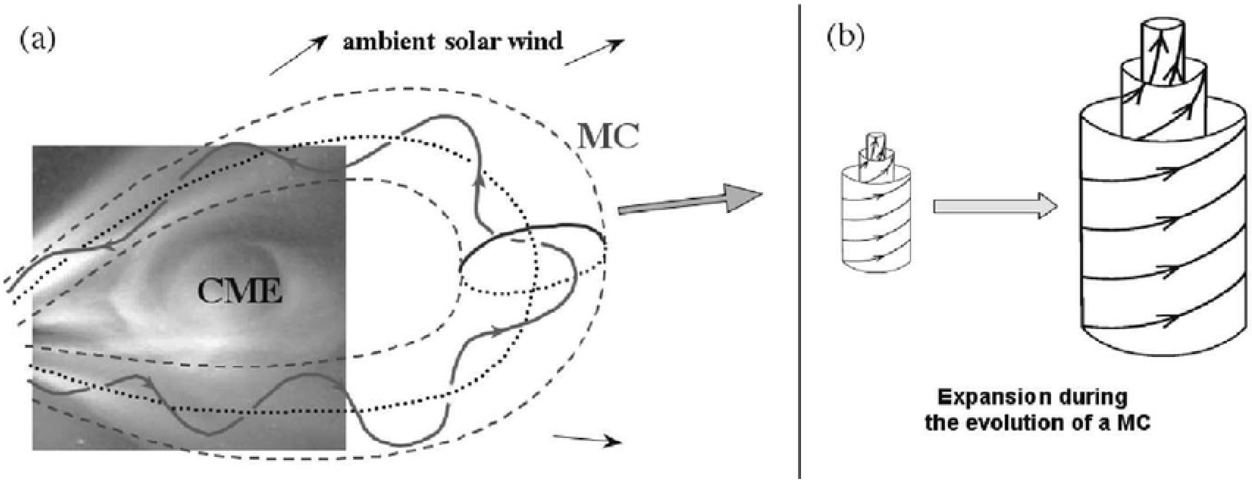

Figure 1.2: (a) Cartoon showing ICME evolution with background solar wind. The LASCO Coronagraph image is superimposed with a flux rope fitting. (b) An ICME column expansion. Image taken from Dasso et al. (2012) [4].

In situ measurements

In situ observations from spacecrafts provide a direct sampling of plasma and field parameters in the ICME cross-section. CMEs with speeds greater than the ambient solar wind drive a shock in front of them. This is followed by a turbulent sheath region (which corresponds to the leading edge in Figure 1.1). ICMEs often carry regions of enhanced smoothly rotating magnetic field components, which are signatures of helical flux rope structures. These are called magnetic clouds (MCs) and are characterized by depressed proton temperatures and low plasma β (ratio of the thermal and magnetic pressures) as compared to the surrounding solar wind plasma (Burlaga et al. (1981) [14]). Figure 1.3 depicts a schematic of a propagating ICME made by Zurbuchen and Richardson (2006) [5], along with the in situ measurements from the WIND Spacecraft (`https://wind.nasa.gov/ICME_catalog/ICME_catalog_viewer.php`) during April 4 – 7, 2010. WIND is located in a halo orbit around the L1 Lagrange point, hence the data is at 1 AU. From top to bottom, the panels show the magnetic field components, total magnetic field, bulk solar wind plasma velocity, proton number density, proton temperature, plasma β and geomagnetic indices $\mathrm{K_p}$ and $\mathrm{D_{st}}$. The black vertical line marks the arrival of shock, followed by the sheath region with enhanced proton density. The two purple lines denote the boundaries of the MC. This region is indicated by increased magnetic field strength with low field variations, reduced T_p and plasma β.

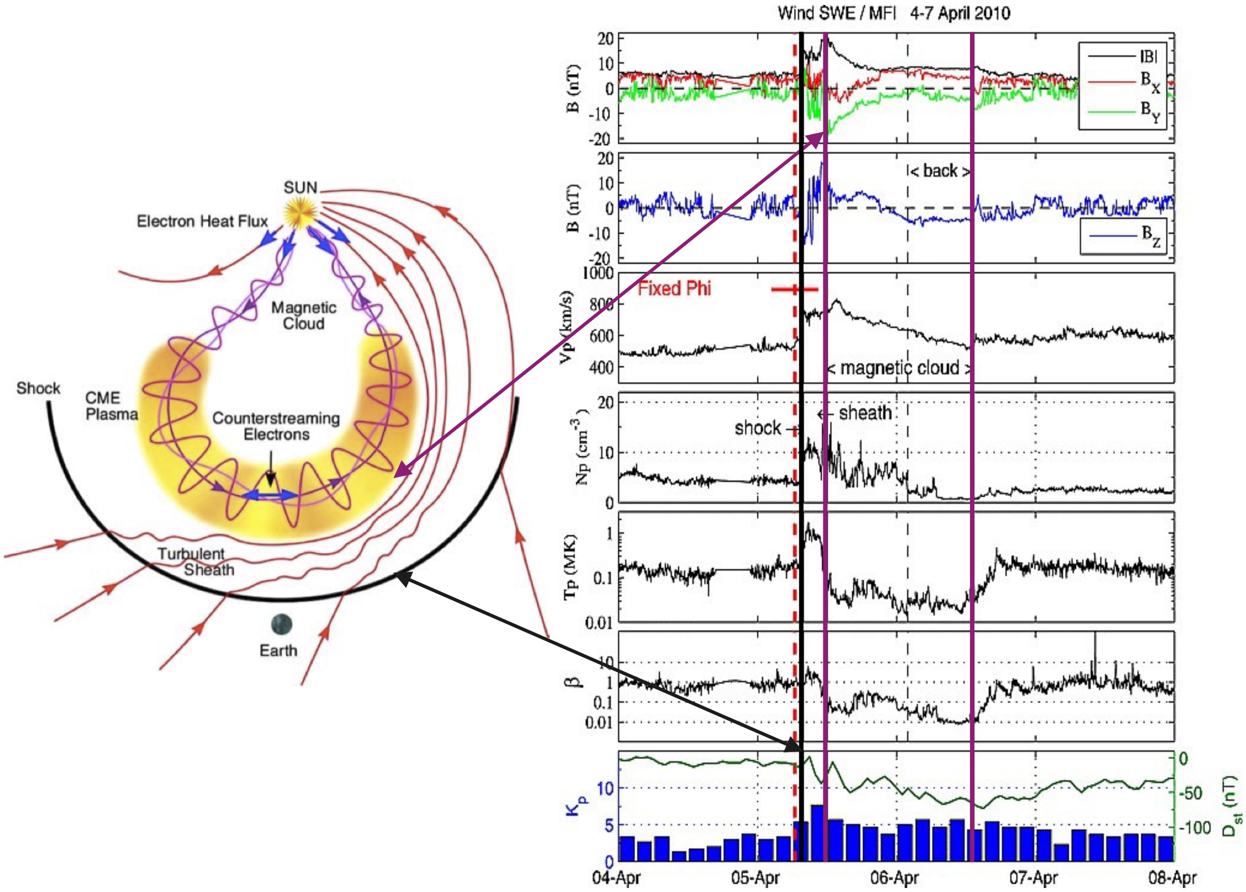

Figure 1.3: ICME Diagram with corresponding in situ properties. The left panel shows a classic ICME schematic (Zurbuchen and Richardson (2006) [5]). The right panel image is taken from Möstl et al. (2010) [6].

1.2 Heating of CMEs

In situ measurements from near-Earth spacecrafts have shown that ICMEs exhibit extremely high plasma temperatures, reaching up to millions of degrees Kelvin, which is much hotter than what would be expected if the plasma parcel expanded adiabatically from the Sun to the Earth.

Several works by Verma et al. (1995) [15], Vasquez et al. (2007) [16] and Chen and Garren (1993) [17] have estimated that a parcel of coronal plasma expanding adiabatically with the solar wind would attain a temperature value as low as a few Kelvin by the time it reaches the Earth. This implies that there has to be some additional heating mechanism inside ICMEs, and our knowledge of CME driving and thermodynamics is incomplete. The explanation for this temperature discrepancy remains inadequate and is an active area of research.

Electron thermal conduction is a potential mechanism for maintaining these high temperatures. We put our focus on electron thermal conductivity since they are the lighter species and are therefore the primary contributors to thermal conduction. The thermal conductivity of protons and heavier species will be substantially lower. In this thesis, we investigate the efficiency of electron thermal conduction along the magnetic field lines connecting the ICME to the solar corona.

1.3 Effects on Space Weather

Space weather can be defined as the varying conditions occurring in the Sun-Earth space environment that may have an impact on the operational efficiency and dependability of space-borne or ground-based systems, and which may also pose a threat to human welfare. The significance of space weather has escalated due to the surging reliance of society on space infrastructure and systems that are susceptible to electromagnetic disturbances and energetic particle radiation (Kilpua et al. (2017) [18]). CMEs are among the most significant drivers of space weather disturbances. They interact with the Earth's magnetosphere to produce geomagnetic storms, which can disrupt radio communication and GPS navigation due to electromagnetic interference. These storms can heat the Earth's upper atmosphere, which increases drag on satellites and shortens their lifespan. CME-induced ring currents can also overload power grids on Earth, leading to blackouts and other electrical disruptions. Additionally, ICME shocks can accelerate solar energetic particles (SEPs), which endanger astronaut safety and severely damage critical spacecraft components by exposing them to high levels of radiation. Given the significant impacts of CMEs on space weather, predicting their occurrence and near-Earth effects is of great importance. By investigating the thermal conduction and electron heating processes in CMEs, this thesis can contribute to improving our understanding of CME dynamics, and thus aid in the development of reliable space weather forecasting techniques for these extreme events.

In the next chapter, we will highlight the motivation for undertaking this study, and briefly outline the thesis organization.

Chapter 2

Motivation and Outline

2.1 Why thermal conduction in CMEs?

This thesis aims to try and re-examine the energy budget for CME dynamics; focusing specifically on the budget for plasma heating inside CMEs.

1. CME dynamics is generally treated in the context of a one-fluid model. There is no distinction between electrons and protons like in two-fluid models, which distinguishes between electron fluid and proton fluid. One-fluid model of the plasma is called Magnetohydrodynamics (MHD) (refer to Section 3.1).

2. The energy available for CME propagation (the energy source is generally thought to be magnetic fields) is usually expended in:

   (a) accelerating the CME

   (b) overcoming aerodynamic drag between the CME and the surrounding solar wind

   (c) heating the CME plasma

3. Why would one even want to consider item 2(c); i.e. plasma heating inside the CME? The answer is pretty much the same as that for a parcel of solar wind: if you consider a parcel of CME plasma that was initially at a million Kelvin, which expands (and cools adiabatically) as it propagates outwards, it will have cooled down to about $3\,\mathrm{K}$ when it reaches

the Earth. But we know, from in situ observations of near-Earth CMEs, that the proton and electron temperatures in the solar wind and inside CMEs are much higher than that - proton temperatures are typically 10^5 K and electron temperatures are often an order of magnitude higher (Section 1.2). So the possibilities are:

(a) The interior of the CME is thermally well connected to the solar corona, allowing for effective heat conduction from the interior. This would be a near-isothermal situation (equivalent to a polytropic index $\gamma \approx 1$), hence alleviating the need for additional CME heating. This would influence CME dynamics because more of the magnetic energy would be available to accelerate the CME and overcome aerodynamic drag.

(b) If the reverse is true; i.e., thermal conduction is inefficient (in which case the polytropic index γ would be close to the adiabatic value of $5/3$), we would need to invoke additional heating mechanisms for energy dissipation within the CME.

We focus on situation 3(a) described above. There is a lot of work dealing with polytropic indices in CMEs and solar wind. Chen (1996) [19] uses a $\gamma \simeq 1.2$ implying relatively high thermal conductivity along the magnetic field connecting the CME to the corona. By performing measurements on different magnetic clouds, Osherovich et al. (1993) [20] obtained a polytropic index between $1.1 < \gamma_p < 1.3$ for protons, and $\gamma_e \approx 0.48 \pm 0.2$ for electrons. Kumar and Rust (1996) [21] use $\gamma = 4/3 \cong 1.33$, which is smaller than the adiabatic value of 5/3. Their results indicate that almost 58% of the magnetic energy is available for ICME heating. Using a collection of 336 ICMEs, Dayeh and Livadiotis (2022) [22] found that polytropic indices vary from $\gamma \simeq 5/3$ upstream of the ICMEs, $\gamma \sim 1.4$ in the sheaths, $\gamma \sim 1.53$ in the ICME ejecta, to $\gamma \simeq 5/3$ again post ICME passage. These results reveal that the turbulent heating rate in the ICME plasma increases when the polytropic index decreases from its adiabatic value to its isothermal value. Another study by Mishra and Wang (2018) [23] found that within near Sun distances of about $15\,\mathrm{R}_\odot$, γ of the CME plasma decreases from 1.8 to 1.35. This suggests initial heat release followed by continuous heat injection. Several studies of solar wind polytropic index have been done. Nicolaou et al. (2020) [24] employed plasma measurements from Parker Solar Probe to examine the large and small-scale variations of the solar wind proton density and temperature at heliocentric distances between $0.17 - 0.8\,\mathrm{AU}$. They conclude that large-scale variations in the heliosphere caused by solar wind expansion tend to follow a polytropic model with $1.5 < \gamma < 5/3$, whereas small-scale fluctuations caused by turbulent compressions follow a polytropic relation with $\gamma \sim 2.7$. A recent work by Dakeyo et al. (2022) [25] determined $\gamma_p \simeq 1.35 - 1.57$ for solar wind protons and $\gamma_e \simeq 1.21 - 1.29$ for solar wind electrons, from temperature and density gradient observations. All of these results seem to have a varied range of implications regarding the thermodynamic evolution of the CME and solar wind plasma.

Rather than addressing polytropic indices, we calculate thermal conduction timescales and derive the velocity of a representative thermal conduction "front". We compare the thermal conduction front velocity with data for CME propagation velocities. If the thermal conduction front is faster than the CME, it would imply that thermal conduction is efficient and vice-versa. This is an alternative approach that can guide and support the choice of a polytropic index in CME propagation models. For instance, is it reasonable to choose $\gamma = 5/3$, or should it be closer to unity? Our findings might help determine the answer.

We use CME propagation velocity data from a sample of 38 well-selected CMEs studied by Sachdeva et al. (2017) [1]. Since electrons are the more mobile species, we use only the electron thermal conduction coefficient. Although it is well known that the solar wind is only weakly collisional (it is certainly so for protons, and true for electrons too, to a lesser extent), we use the standard Spitzer collisional mean free path to compute electron thermal conductivity. In addition, we also determine anomalous (i.e., non-Spitzer) electron thermal conductivity using a modified collisional mean free path that takes into account additional scattering due to turbulence.

2.2 Thesis Organization

Below we briefly outline the structure for the rest of the thesis:

- **Chapter 3** provides a detailed overview of the necessary theoretical background of MHD equations, Spitzer electron thermal conduction and how it gets modified via turbulent fluctuations of the magnetic field. We also briefly discuss how we approximate the density, temperature and magnetic field inside CMEs using an empirical solar wind model.
- **Chapter 4** describes the datasets used in this thesis and the procedures employed to estimate the CME propagation velocity.
- **Chapter 5** discusses the results obtained from the study on electron thermal conduction in CMEs, with relevant explanations for the observations.
- **Chapter 6** concludes and summarizes these results and suggests scopes for future work.
- **Chapter 7** is the appendix which contains a formula table and additional plots.

Chapter 3

Methodology

3.1 Introduction to Magnetohydrodynamics (MHD)

Magnetohydrodynamics (MHD) is a mathematical framework used to describe the behaviour of plasma as an electrically conducting fluid under the influence of magnetic fields. In MHD, the plasma is treated as a fluid with macroscopic parameters like density, pressure, temperature and flow speed influenced by electric and magnetic forces. Essentially, the equations governing MHD are a reduction of the laws of fluid dynamics coupled with Maxwell's equations of electrodynamics.

3.1.1 The MHD Approximation

The assumptions of the MHD approximation are:

- The fluid approximation
- *Ohm's law*, which is a local, instantaneous relationship between electric field and current density, holds true in the plasma.
- The plasma is electrically neutral over macroscopic lengthscales.

The basic equations of MHD include the continuity equation, which describes the conservation of mass, the momentum equation, which describes the conservation of momentum, the induction equation, which describes the evolution of the magnetic field and the energy equation which deals with the conservation of energy. We will first introduce the ideal MHD equations and then extend them to include resistive effects. We will use CGS units throughout this thesis.

3.1.2 Ideal MHD

The ideal MHD equations are a set of coupled differential equations that describe the behaviour of a plasma in the absence of resistive effects. Thus, ideal MHD assumes that the fluid is infinitely conducting. In CGS units, the ideal MHD equations are given by (e.g., Choudhuri et al. (1998) [26]):

Continuity equation:

$$\frac{\partial \rho}{\partial t} + \nabla \cdot (\rho \mathbf{v}) = 0 \tag{3.1}$$

Momentum equation:

$$\frac{\partial \mathbf{v}}{\partial t} + (\mathbf{v} \cdot \nabla)\mathbf{v} = -\frac{1}{\rho}\nabla p + \frac{\mathbf{F}}{\rho} + \frac{1}{\rho c}\mathbf{j} \times \mathbf{B} \tag{3.2}$$

Induction equation:

$$\frac{\partial \mathbf{B}}{\partial t} = \nabla \times (\mathbf{v} \times \mathbf{B}) \tag{3.3}$$

Energy equation:

$$\frac{\partial E}{\partial t} = -\nabla \,.\, \left[\frac{\rho v^2}{2}\mathbf{v} + \frac{\gamma}{\gamma - 1} p\,\mathbf{v} - \frac{(\mathbf{v} \times \mathbf{B}) \times \mathbf{B}}{4\pi}\right] \tag{3.4}$$

Here, ρ is the plasma mass density ($\mathrm{g\,cm^{-3}}$), $\mathbf{v}$ is the plasma velocity ($\mathrm{cm\,s^{-1}}$), p is the plasma pressure ($\mathrm{dyne\,cm^{-2}}$), $\mathbf{F} = -\rho \mathbf{g}$ is the body force density ($\mathrm{dyne\,cm^{-3}}$), $\mathbf{B}$ is the magnetic field (G), $\mathbf{j} = \frac{c}{4\pi}\nabla \times \mathbf{B}$ is the current density, c is the speed of light ($\mathrm{cm\,s^{-1}}$), E is the energy density ($\mathrm{erg\,cm^{-3}}$) and γ is the polytropic index. The term in square brackets on the RHS of Equation 3.4

represents the total energy flux ($\mathrm{erg\,cm^{-2}\,s^{-1}}$) of the magnetized fluid.

3.1.3 Resistive MHD

In resistive MHD, all dissipative processes like finite viscosity, electrical resistivity and thermal conductivity are taken into account. The continuity equation for resistive MHD remains unchanged. The rest of the equations are given by (e.g., Priest (1984) [27]):

Momentum equation:

$$\frac{\partial \mathbf{v}}{\partial t} + (\mathbf{v}\cdot\nabla)\mathbf{v} = -\frac{1}{\rho}\nabla p + \frac{\mathbf{F}}{\rho} + \frac{1}{\rho c}(\mathbf{j}\times\mathbf{B}) + \nu\nabla^2\mathbf{v} \tag{3.5}$$

Induction equation:

$$\frac{\partial \mathbf{B}}{\partial t} = \nabla\times(\mathbf{v}\times\mathbf{B}) + \eta\nabla^2\mathbf{B} \tag{3.6}$$

Energy equation:

$$\frac{\partial E}{\partial t} + \nabla .\left[\frac{\rho v^2}{2}\mathbf{v} + \frac{\gamma}{\gamma-1}p\,\mathbf{v} - \frac{(\mathbf{v}\times\mathbf{B})\times\mathbf{B}}{4\pi}\right] = -\mathcal{L} \tag{3.7}$$

Here, the momentum equation includes the viscous term, where ν is the coefficient of kinematic viscosity. In the induction equation, η is called the magnetic diffusivity and is defined as $\eta = \frac{c^2}{4\pi\sigma}$, where σ is the electrical conductivity of the plasma.

The energy equation in resistive MHD includes an additional term $\mathcal{L}$ which is the energy loss/gain function defined as:

$$\mathcal{L} = \nabla\cdot\mathbf{q} + L_{\mathrm{r}} - \frac{j^2}{\sigma} - \mathcal{H} \tag{3.8}$$

where, $\mathbf{q}$ is the heat flux due to the thermal conduction, L_{r} is the radiation function, $\frac{j^2}{\sigma}$ is the Ohmic dissipation, and $\mathcal{H}$ represents the sum of all the other heating sources.

3.2 Electron Thermal Conduction inside CMEs using Spitzer Conductivity

As mentioned in the previous chapters, thermal conduction from the sun along the magnetic field can help to explain the observed electron temperature at 1 AU. We now briefly outline an estimate of electron thermal conductivity.

The electron-electron collisional timescale τ_{ee}, is defined as the average time for collisions between electrons in the plasma over which the velocity distribution of the electrons relax to a Maxwellian distribution (Spitzer (1962) [28]). The collisions are usually attributed to Coulomb collisions in a collision-dominated plasma, and we first consider this scenario. However, the plasma comprising the solar wind and CMEs is only marginally collisional (by way of Coulomb collisions). Turbulent magnetic field irregularities can act as scattering centers and mediate electron collisions. We consider Coulomb collisions here and examine the effect of turbulence mediated collisions later in Section 3.3. The electron-electron collisional timescale due to Coulomb collisions is (Spitzer (1962)):

$$\tau_{ee} = \frac{m_e^{1/2}\, 3\, k_{\mathrm{B}}^{3/2}}{8 \times 0.714\, \pi\, e^4} \frac{T_e^{\,3/2}}{n_e\, \ln \Lambda} = 2.66 \times 10^{-1} \frac{T_e^{\,3/2}}{n_e\, \ln \Lambda} \tag{3.9}$$

where m_e is the electron mass, $k_{\mathrm{B}} = 1.380649 \times 10^{-16}$ $(\mathrm{erg\,K^{-1}})$ is the Boltzmann constant, e is the elementary charge (in e.s.u.), n_e is the electron number density, $T_e\,(\mathrm{K})$ is the electron temperature, and $\ln \Lambda\,(\approx 20)$ is the Coulomb logarithm (refer to Table 7.1). τ_{ee} is in units of second. We can obtain the proton-proton collisional timescale and the electron-proton collisional timescale by multiplying equation 3.9 by a factor of $\sqrt{m_p/m_e}$ and m_p/m_e respectively (Boyd and Sanderson, Sturrock (2003, 1994) [29, 30]).

In a plasma, thermal conductivity is due to collisions between the constituent particles. From the energy equation in resistive MHD (Equation 3.7), we have the energy loss/gain function term $\mathcal{L}$. The heating term in Equation 3.8 can be expanded using Fourier's law of thermal conduction, which states that the thermal heat flux $\mathbf{q}$ is proportional to the temperature gradient ∇T. From the differential form of Fourier's law of thermal conduction,

$$\mathbf{q} = -\kappa \nabla T \tag{3.10}$$

This equation relates the heat flux $\mathbf{q}$ to the temperature gradient ∇T via a constant of proportionality κ, called the coefficient of thermal conductivity, or simply thermal conductivity.

Spitzer (1962) thermal conductivity of electrons can be expressed as

$$\kappa = \frac{5 n_e k_{\mathrm{B}}^2 T_e}{2 m_e} \tau_{ee} \tag{3.11}$$

We are concerned only with electron thermal conduction because electrons are the primary species responsible for thermal conduction in a plasma due to their low mass and relatively high mobility.

The thermal conduction timescale is the effective time over which thermal conduction occurs. It is generally estimated by dividing the thermal energy by the divergence of the heat flux ($\nabla \mathbf{q}$). To calculate the local electron thermal conduction timescale, we use the following formula:

$$\tau_{cond} = \frac{21}{5} \frac{n_e k_{\mathrm{B}} L^2}{\kappa} \tag{3.12}$$

This equation is taken from *Physics of the Solar Corona* by Aschwanden (2005) [3]. This formula is used in flare-loop studies. Here, κ is in $(\mathrm{erg\,s^{-1}\,cm^{-1}\,K^{-1}})$, $L\,(\mathrm{cm})$ is the relevant lengthscale over which the temperature varies. τ_{cond} is in units of second. From equation 3.10, we can see that thermal conductivity κ appears alongside ∇T, which is essentially $\frac{dT}{dr}$ in one-dimension. Hence the lengthscale can be calculated as:

$$L = \left| \left[\frac{1}{T} \frac{dT}{dr} \right]^{-1} \right| \tag{3.13}$$

Here, r represents the Sun-centered distance or heliocentric distance in units of $\mathrm{cm}, \mathrm{R}_{\odot}$ or AU.

To quantify the degree of electron thermal conduction inside CMEs, it is useful to define the velocity of a *thermal conduction front* by:

$$V_{cond} = \frac{L}{\tau_{cond}} \tag{3.14}$$

This quantity represents the speed at which a thermal packet propagates (in $\mathrm{cm\,s^{-1}}$).

Now, in order to determine whether electron thermal conduction from the Sun to Earth for ICMEs is efficient or not, we will compare the thermal conduction velocities of a range of ICMEs with their corresponding Sun-Earth propagation velocities. If the thermal conduction front is propagating faster than the ICME, it would imply that thermal conduction is efficient and vice-versa.

3.3 Electron Thermal Conduction inside CMEs using non-Spitzer Conductivity

Turbulent diffusion can significantly affect the thermal conduction rates inside CME plasma. Since transport phenomenon like thermal conduction is a consequence of the Coulomb collisions, turbulent scattering can affect the collisional timescales of electrons and protons.

Small-scale fluctuations carried by a large-scale background magnetic field are responsible for MHD turbulence. Charged particles like electrons gyrate around the background magnetic field in the absence of turbulence. In the presence of turbulence, these particles are stochastically scattered by turbulent fluctuations in the magnetic field. One can think of this as electrons colliding with magnetic scattering centers. This leads to electron diffusion in both parallel and perpendicular directions to the magnetic field.

To calculate the turbulent diffusion coefficient of electrons, Bhattacharjee et al. (2023) [31] have used the findings of Candia and Roulet (2004) [32] on charged particle dynamics in a turbulent plasma. Candia and Roulet's simulations yielded fitting formulae for particle diffusion coefficients of high energy cosmic rays, and are applicable to particles of any energy range. For the case of near-Earth MCs, the modified fitting formula for the electron turbulent diffusion coefficient ($\mathrm{cm}^2\,\mathrm{s}^{-1}$) parallel to the large-scale background magnetic field is given as (Bhattacharjee et al., Candia and Roulet (2023, 2004)):

$$D_{\|} = v_{T_e} L_{max} \rho \times \frac{N_{\|}}{(\delta B/B)^2} \times \sqrt{\left(\frac{\rho}{\rho_{\|}}\right)^{2(1-\Gamma)} + \left(\frac{\rho}{\rho_{\|}}\right)^2} \tag{3.15}$$

Here, v_{T_e} ($\mathrm{cm\,s^{-1}}$) is the electron thermal velocity, L_{max} (cm) is the maximum turbulent lengthscale of the system, $\rho = \frac{R_e}{L_{max}}$ is the ratio of the electron gyroradius ($R_e = 2.21 \times 10^{-2}\, T_e^{1/2}\, B^{-1}\,\mathrm{cm}$) (see Table 7.1) to L_{max}, and it is a measure of how tightly the particle is bound to the magnetic field. We will take L_{max} to be equal to the temperature gradient lengthscale L (from Equation 3.13). The quantity $\delta B/B$ represents the average value of the total magnetic field modulation index inside a given near-Earth CME. Using a sample of 152 near-Earth MCs, Bhattacharjee et al. (2023) found the average value of $\delta B/B$ inside the MCs to be around 0.044. We will assume that $\delta B/B = 0.044$ throughout the course of the Sun-Earth propagation of CMEs. The constants Γ, $N_{\|}$ and $\rho_{\|}$ are fitting parameters that depend upon the type of the turbulent energy spectra. Turbulent diffusion can be modelled by considering the energy cascade from large to small scales, and is usually described by two different types of turbulence spectra, namely *Kolmogorov* and *Kraichnan* spectra.

Kolmogorov Spectrum

While Kolmogorov phenomenology (Kolmogorov (1941) [33]) was developed to explain incompressible hydrodynamic turbulence, it can also be used to explain magnetic fluctuations in the solar wind and ICMEs (Leamon et al. (1998) [34]). The turbulent energy per unit mass per unit wavenumber (k) is given as (Liu et al. (2006) [35]):

$$E_{\text{ko}}(k) = C_{\text{ko}} \epsilon^{2/3} k^{-5/3} \tag{3.16}$$

where $C_{\text{ko}} \simeq 1.6$ and ϵ is the energy transfer rate. In this case, the energy cascade is scale-invariant and the turbulence spectrum follows a power-law distribution. Kolmogorov spectrum corresponds to a weak magnetic field limit. The appropriate values of the parameters in Equation 3.15 for the Kolmogorov spectrum are $\Gamma = 5/3$, $N_{\parallel} = 1.7$ and $\rho_{\parallel} = 0.2$ (see Table 1 of Candia and Roulet (2004)).

Kraichnan Spectrum

The Kolmogorov theory was modified by Kraichnan (1965) [36] to include the effect of magnetic fields. The MHD turbulence spectrum is given by (Biskamp (1993) [37]):

$$E_{\text{kr}}(k) = C_{\text{kr}} (\epsilon\, v_A)^{1/2} k^{-3/2} \tag{3.17}$$

where $C_{\text{kr}} = C_{\text{ko}}^{3/4} \simeq 1.42$ and v_A is the alfvén velocity. In the case of Kraichnan turbulence, the energy cascade is anisotropic and it applies to the case of strong magnetic fields. For the parameter values, we use $\Gamma = 3/2$, $N_{\parallel} = 2$ and $\rho_{\parallel} = 0.22$ which are applicable to Kraichnan turbulence.

Velocity fluctuations in the solar wind have been observed to follow the Kraichnan spectrum (Vasquez et al., Podesta et al., Podesta and Borovsky, Borovsky (2007, 2007, 2010, 2012) [16, 38–40]), while the magnetic field fluctuations in the solar wind and ICMEs obey the Kolmogorov scaling (Liu et al., Salem et al., Roberts, Alexandrova et al. (2006, 2009, 2010, 2013) [35, 41–43]). Since we do not know the exact mechanism through which turbulent dissipation occurs inside

CMEs, we will use both forms of the turbulent energy spectra for our calculations of the anomalous electron thermal conductivity.

3.3.1 Calculation of Anomalous (non-Spitzer) Conductivity

By incorporating the values of magnetic field fluctuations inside near-Earth MCs obtained by Bhattacharjee et al. (2023), as well as the specific parameters for the form of turbulence in Equation 3.15, we can extract the effective anomalous electron (non-Spitzer) diffusion timescale (in seconds) as:

$$\tau_{ee}^{nsp} = \frac{D_{\parallel}}{v_{T_e}^2} \quad , \tag{3.18}$$

Instead of the usual Spitzer or Coulomb collision timescale (Equation 3.9), we can now use this modified timescale to determine an anomalous (non-Spitzer) thermal conductivity for the electrons inside the CME plasma as:

$$\kappa_{nsp} = \frac{5 n_e k_{\mathrm{B}}^2 T_e}{2 m_e} \tau_{ee}^{nsp} \tag{3.19}$$

The anomalous electron thermal conduction timescale is given by:

$$\tau_{cond}^{nsp} = \frac{21}{5} \frac{n_e k_{\mathrm{B}} L^2}{\kappa_{nsp}} \tag{3.20}$$

It follows from Equations 3.20 and 3.14 that the anomalous electron thermal conduction front velocity $(\mathrm{cm\,s^{-1}})$ is:

$$V_{cond}^{nsp} = \frac{L}{\tau_{cond}^{nsp}} \tag{3.21}$$

We will now describe how to get the values of CME properties such as n_e, T_e, B throughout its interplanetary propagation by using an empirical average solar wind model.

3.4 CME Parameter Values from Solar Wind Model

Since we are interested in quantifying the thermal conductivity of a CME propagating through the heliosphere, we need the values for CME plasma parameters like density, temperature and magnetic field throughout the duration of its propagation. However, these values are available only at certain **specific** heliocentric distances via in situ measurements made by several spacecrafts. However, since we need the evolution of the physical parameters of a CME throughout its propagation, we will use empirical formulas from the Venzmer and Bothmer (2018) [44] Solar Wind Model.

Using in situ observations from Space-borne coronagraphs and probes, Venzmer and Bothmer (2018) developed an empirical solar-wind model for the inner heliosphere by combining the solar activity relationships of the solar wind frequency distributions and their distance dependencies. The derived formulae for the average solar wind proton density, temperature and magnetic field strength as a function of heliocentric distance r are:

$$n_p = 1.305\,(0.0038 \cdot ssn + 4.5)\, {r_{\mathrm{AU}}}^{-2.11} \ \ \mathrm{cm}^{-3} \tag{3.22}$$

$$T_p = 1.654\,(197 \cdot ssn + 57300)\, {r_{\mathrm{AU}}}^{-1.1} \ \ \mathrm{K} \tag{3.23}$$

$$B = 1.0879 \times 10^{-5}\,(0.0131 \cdot ssn + 4.29)\, {r_{\mathrm{AU}}}^{-2.11} \ \ \mathrm{G} \tag{3.24}$$

Here, r_{AU} is the normalized heliocentric distance in AU and ssn is the yearly averaged sunspot number. The international sunspot number can be accessed from the online database at the World Data Center - Sunspot Index and Long-term Solar Observations (WDC-SILSO) (`https://www.sidc.be/silso/datafiles`).

In order to calculate the CME electron thermal conduction timescale, we have made the following assumptions:

1. Electron number density = Proton number density, i.e. $n_e = n_p$
2. Electron temperature = $10 \times$ Proton temperature, i.e. $T_e = 10\,T_p$

The first assumption is a straightforward consequence of the electrical neutrality assumption from the MHD approximation in Subsection 3.1.1. We have made the second assumption because electron velocity moment data from the WIND spacecraft is not calibrated and thus is not in an usable format. We, therefore assumed that the electron temperature exceeds the proton temperature by a factor of 10 as prescribed by Osherovich et al. (1993) [20] and used by Bhattacharjee et al. (2022) [2].

Applying these assumptions and converting r_{AU} to r (cm) gives us:

$$n_e = (0.004959 \cdot ssn + 5.8725)\,(6.297 \times 10^{27})\,r^{-2.11}\ \mathrm{cm}^{-3} \tag{3.25}$$

$$T_e = (3258.38 \cdot ssn + 947742)\,(3.108 \times 10^{14})\,r^{-1.1}\ \mathrm{K} \tag{3.26}$$

$$B = 1.0879 \times 10^{-5}\,(0.0131 \cdot ssn + 4.29)\,(7.4197 \times 10^{21})\,r^{-2.11}\ \mathrm{G} \tag{3.27}$$

From Equations 3.13 and 3.26, the relevant lengthscale is calculated as:

$$L = \left|\left[\frac{1}{T_e}\frac{dT_e}{dr}\right]^{-1}\right| = \frac{1}{1.1} r\ \mathrm{cm} \tag{3.28}$$

Using equations 3.25 – 3.28, we will evaluate the electron thermal conductivity for a CME as it propagates through the heliosphere.

Chapter 4

Data and Analysis

4.1 CME Velocity using GCS fitted data

CMEs are observed as white light images in the coronagraph field of view (FOV) using various instruments onboard the SOHO (*Solar and Heliospheric Observatory*) and STEREO (*Solar Terrestrial Relations Observatory*) spacecrafts. SOHO carries the *Large Angle and Spectrometric Coronagraph* (LASCO) C2 with a FOV of 1.5 – 6 $R_\odot$. The list of all CMEs observed by LASCO is available in the SOHO/LASCO CME Catalog (`https://cdaw.gsfc.nasa.gov/CME_list/`).

SECCHI (*Sun–Earth Connection Coronal and Heliospheric Investigation*) onboard STEREO is a suite of 5 scientific telescopes that observe the solar corona and inner heliosphere up to the interplanetary medium. STEREO A and B, taken with the coronagraph COR1 (FOV 1.4 – 4 $R_\odot$) and heliospheric imager HI1 (FOV 12 – 318 $R_\odot$) in SECCHI can track the CME evolution as it propagates through the heliosphere. The image data from two viewpoints of A and B can be accessed from SECCHI Data (`https://secchi.nrl.navy.mil/`).

Using observational data from SOHO LASCO C2, STEREO SECCHI COR2 A/B and HI1, Sachdeva et al. (2017) [1] shortlisted a set of 38 well-observed Earth-directed CMEs. These events provide continuous tracking of CMEs from near-Sun ($\sim 3\,R_\odot$) to interplanetary distances (up to and beyond $80\,R_\odot$). The images from all of these events are fitted using the *Graduated Cylindrical Shell* (GCS) geometrical model. This model fits a three-dimensional helical flux rope structure to observable CMEs for all time stamps from the initial appearance of CME in LASCO C2 to the HI1 FOV.

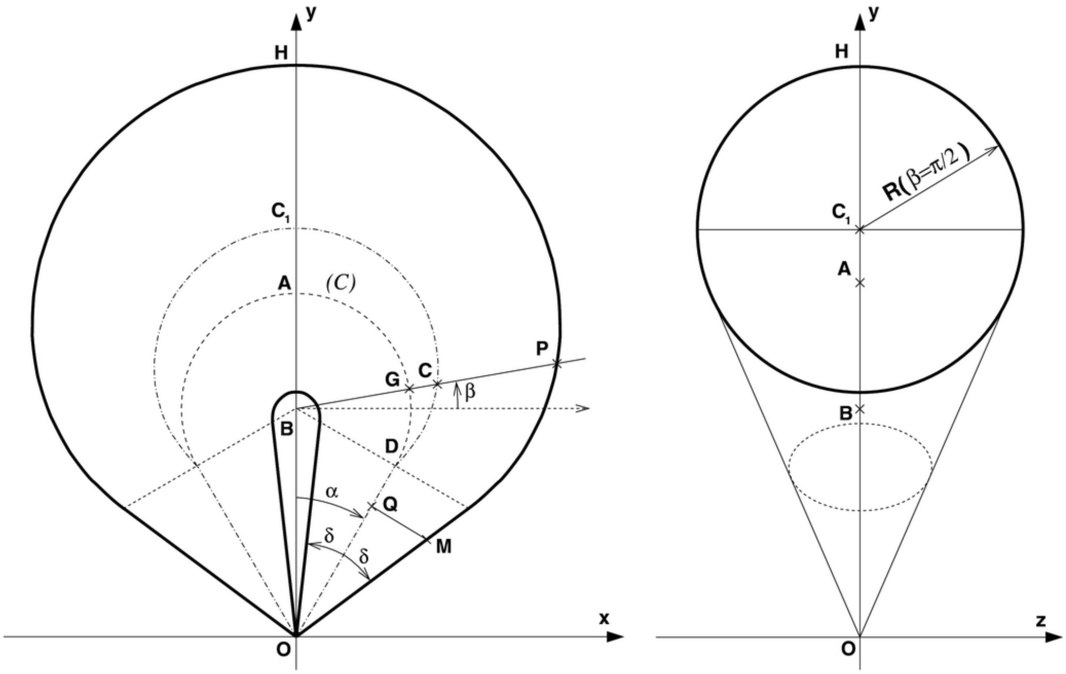

(a) (b)

Figure 4.1: Schematic diagram to represent the GCS model geometry in (a) face-on view and (b) edge-on view. This image is taken from Thernisien (2011) [7].

Figure 4.1 shows the geometric picture of the GCS model by Thernisien (2011) [7]. The left panel depicts a planar section of the face-on view and the right panel depicts a planar section of the edge-on view. In this model, a CME is visualised as two conical legs rooted in the Sun, with the front as a torus with expanding cross-section. Point **O** is the centre of the Sun.

Using the GCS model prescription, Sachdeva et al. (2017) have obtained observational parameters like the CME leading edge height $h\,(\mathrm{R}_\odot)$ for all of the 38 events beginning from LASCO C2, COR2 A & B, to HI1 at each time-stamp. Their CME data list contains derived height and time values for each event. The CME leading edge height h is the measure of the heliocentric distance of the CME leading edge from the centre of the Sun; i.e. $h = r$. Time t is the corresponding time stamp in seconds ($t = 0$ indicates the first time stamp at which the GCS fit is done simultaneously in C2 and COR2 A/B). Essentially, t represents the CME propagation time at a specific value of h; i.e. $t = \tau_{prop}$. Therefore, we can use the height-time evolution data for each of the 3D reconstructed CMEs to analyze their dynamics and propagation.

In order to determine the propagation velocity of each CME at all distances, we numerically differentiate the leading edge height h with respect to the corresponding time stamp t. This is done by using the numpy.gradient function in Python (`https://numpy.org/doc/stable/reference/generated/numpy.gradient.html`). The advantage is that, unlike normal numerical differentiation which has one less element per h value, each value of the derivative $\frac{dh}{dt}$ has the same shape as h.

For h in km, the CME velocity in $\mathrm{km\,s^{-1}}$ is given as:

$$V_{\mathrm{CME}} = \frac{dh}{dt} \tag{4.1}$$

One point to note is that this approach of calculating the CME velocity is quite different from what was used by Sachdeva et al. (2017). They fitted the h vs t plots using a third-order polynomial and then differentiated the fitted plot to derive the CME velocity. Our approach varies in this regard as we are not performing any polynomial fit and hence the velocity we obtain has much more scatter.

Table 4.1 lists the details of the sample of 38 CMEs studied by Sachdeva et al. (2017). Column 1 corresponds to the serial number of the events, and the same number is used throughout the thesis. The 18 CMEs marked with a superscript of f represent fast CMEs with initial velocity $> 900\,\mathrm{km\,s^{-1}}$. We have also identified a list of 15 WIND ICME events from Bhattacharjee et al. (2022), marked with an asterisk *. These events manifest as magnetic clouds (MCs) in the near-Earth environment. The data can be accessed from the WIND ICME Catalogue (`https://wind.nasa.gov/ICMEindex.php`). Column 2 is the date on which the CME was first observed in LASCO C2. The 3rd column gives the year-averaged mean sunspot number (ssn) corresponding to the observation year. h_0 is the first observed CME leading edge height of the GCS fit, and V_0 is the derived CME velocity using the method described above. The 6th column lists the average in situ MC velocity obtained from the WIND spacecraft data for the 15 events. Since WIND is situated at the L1 Lagrange point of the Sun-Earth system, V_{MC} is essentially the average CME velocity at $\approx 213\,\mathrm{R}_{\odot}$.

The velocity vs distance profiles for some of these CMEs are shown in the next chapter. The plots show a comparison of V_{CME}, V_{cond} and V_{cond}^{nsp} as a function of heliocentric distance r. For the WIND events, We have also included V_{MC} in the profiles.

Table 4.1: List of the 38 CMEs shortlisted by Sachdeva et al. (2017) [1] for the period of March 2010 to December 2013. Fast CMEs are designated by a superscript f. The 15 events indicated with an asterisk (*) coincide with the near-Earth counterparts of WIND events from Table A.1 of Bhattacharjee et al. (2022) [2].

CME No.	Date	ssn	$\mathbf{h_0}$ ($\mathrm{R_\odot}$)	$\mathbf{V_0}$ ($\mathrm{km\,s^{-1}}$)	$\mathbf{V_{MC}}$ ($\mathrm{km\,s^{-1}}$)
1^*	2010 March 19	24.9	3.5	162	292.2
2^{*f}	2010 April 3	24.9	5.5	916	635.2
3^*	2010 April 8	24.9	2.9	468	411.4
4^*	2010 June 16	24.9	5.7	193	361.5
5^*	2010 September 11	24.9	4.0	444	371.0
6^*	2010 October 26	24.9	5.3	215	341.6
7	2010 December 23	24.9	3.7	147	
8	2011 January 24	80.8	4.4	276	
9	2011 February 15	80.8	4.4	832	
10	2011 March 3	80.8	4.9	349	
11^*	2011 March 25	80.8	4.8	47	344.3
12	2011 April 8	80.8	4.7	300	
13	2011 June 14	80.8	3.6	562	
14^f	2011 June 21	80.8	8.4	1168	
15^f	2011 July 09	80.8	4.1	903	
16^f	2011 August 4	80.8	7.3	1638	
17^*	2011 September 13	80.8	3.8	493	443.7
18^f	2011 October 22	80.8	4.0	1276	
19	2011 October 26	80.8	7.8	889	
20	2011 October 27	80.8	5.3	882	
21^f	2012 January 19	84.5	4.6	1823	
22^f	2012 January 23	84.5	4.0	1910	
23^f	2012 January 27	84.5	3.5	2397	
24^f	2012 March 13	84.5	3.9	1837	
25	2012 April 19	84.5	4.1	648	
26^{*f}	2012 June 14	84.5	6.2	1152	449.1
27^{*f}	2012 July 12	84.5	4.4	1248	491.1
28^f	2012 September 28	84.5	6.7	1305	
29^*	2012 October 5	84.5	4.4	461	397.7
30^*	2012 October 27	84.5	7.3	380	340.3
31^*	2012 November 9	84.5	3.8	602	381.2
32	2012 November 23	84.5	6.3	492	
33^{*f}	2013 March 15	94.0	4.7	1504	529.0
34^{*f}	2013 April 11	94.0	5.9	1115	390.8
35^f	2013 June 28	94.0	6.6	1637	
36^f	2013 September 29	94.0	4.9	1217	
37^f	2013 November 7	94.0	5.9	975	
38^f	2013 December 7	94.0	6.8	1039	

Chapter 5

Results and Discussion

In this chapter, we will summarize and discuss the results from our study of electron thermal conduction in CMEs. Using the given expressions, assumptions and datasets, we have calculated CME parameters like n_e, T_e, B, and subsequently used them to determine the electron collisional and conduction timescales, conduction front velocities and CME propagation speeds for the 38 events. We then show plots of timescales, velocities and proton heating rates as the CME evolves for both Spitzer and non-Spitzer thermal conductivities. The x-axis in all of the following plots represents the heliocentric distance r of the CME leading edge in $\mathrm{R}_{\odot}$. The y-axis for all of the plots is in the logarithmic scale. The profiles for two representative CMEs, namely CME2 and CME11 are highlighted since they are among the few instances of CMEs that have been tracked continuously from the Sun to the Earth till near-Earth distances of $\approx 210\,\mathrm{R}_{\odot}$.

5.1 Timescale vs Distance Plots

We will start by looking at plots of all the different timescales vs r. We have plotted 5 timescales as a function of r in Figures 5.1 – 5.3. Equations 3.9 and 3.18 give us the electron collision time τ_{ee}, which is then multiplied by a factor of $\sqrt{m_p/m_e}$ and m_p/m_e to obtain τ_{pp} and τ_{ep} respectively. Equations 3.12 and 3.20 give us the thermal conduction timescales, while τ_{prop} is simply the time taken for the CME leading edge to reach r.

5.1.1 Spitzer Timescale Profiles

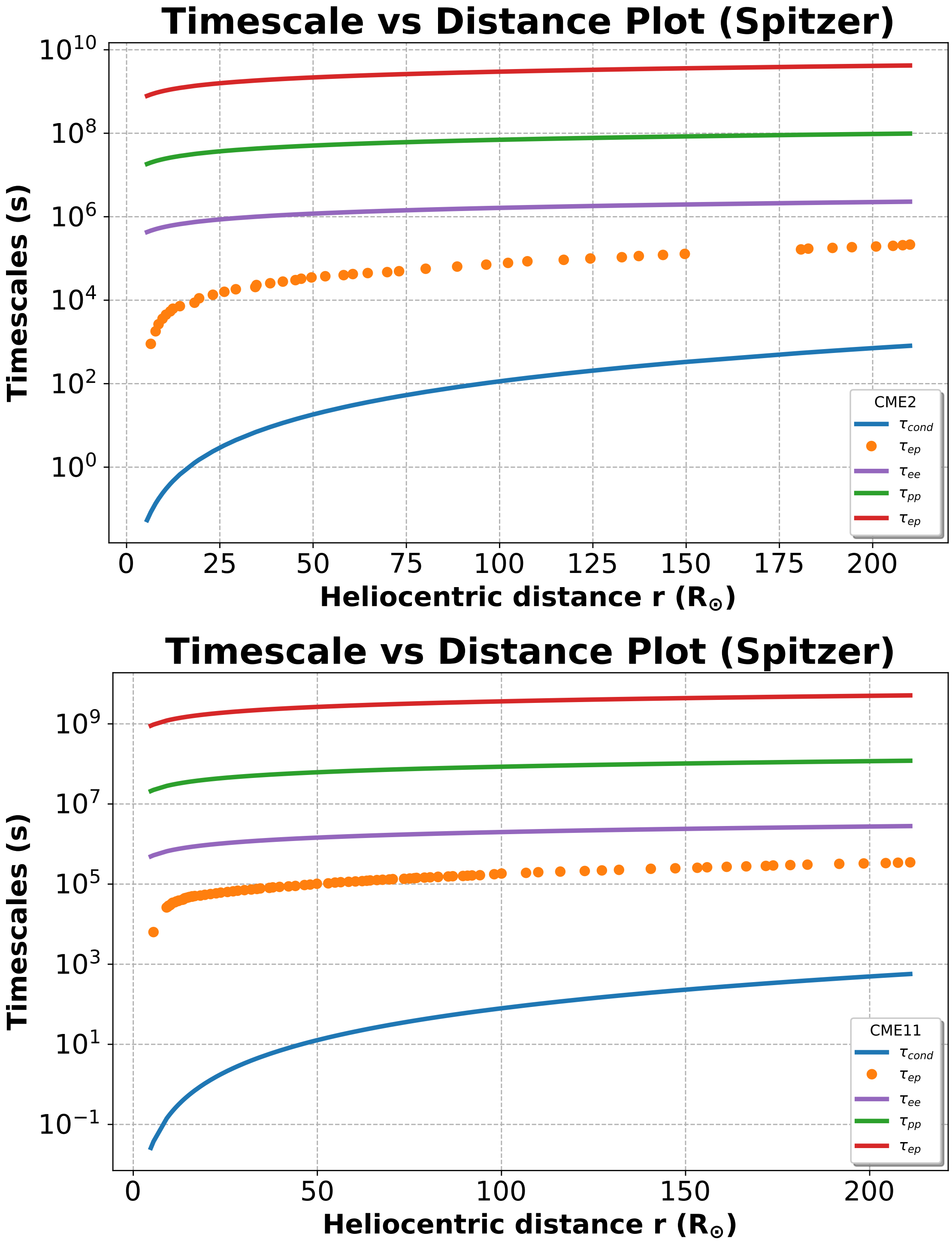

Figure 5.1: Spitzer Timescales vs Distance Plots for CME2 and CME11

5.1.2 Non-Spitzer Timescale Profiles

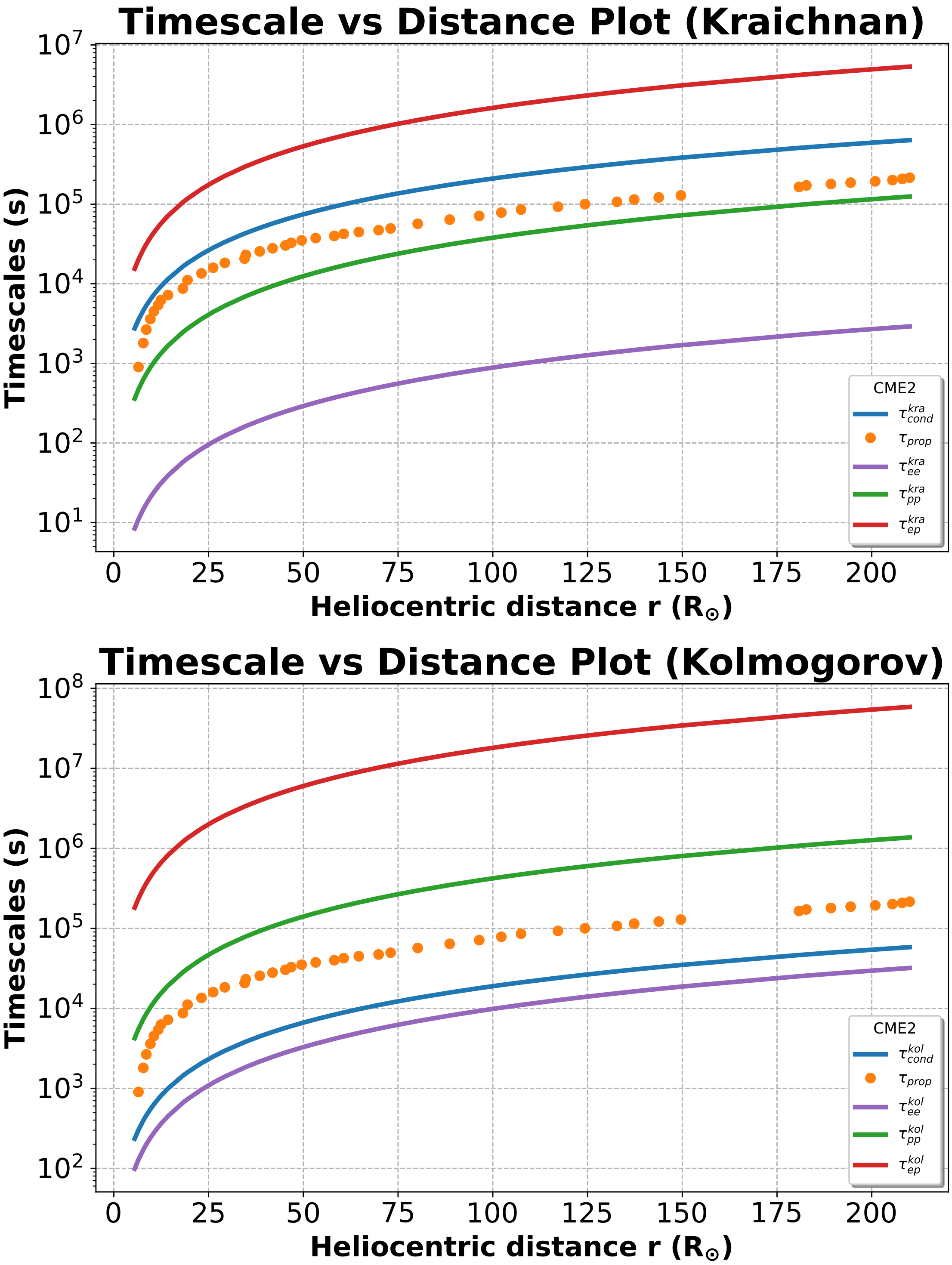

Figure 5.2: Non-Spitzer Timescales vs Distance Plots for CME2

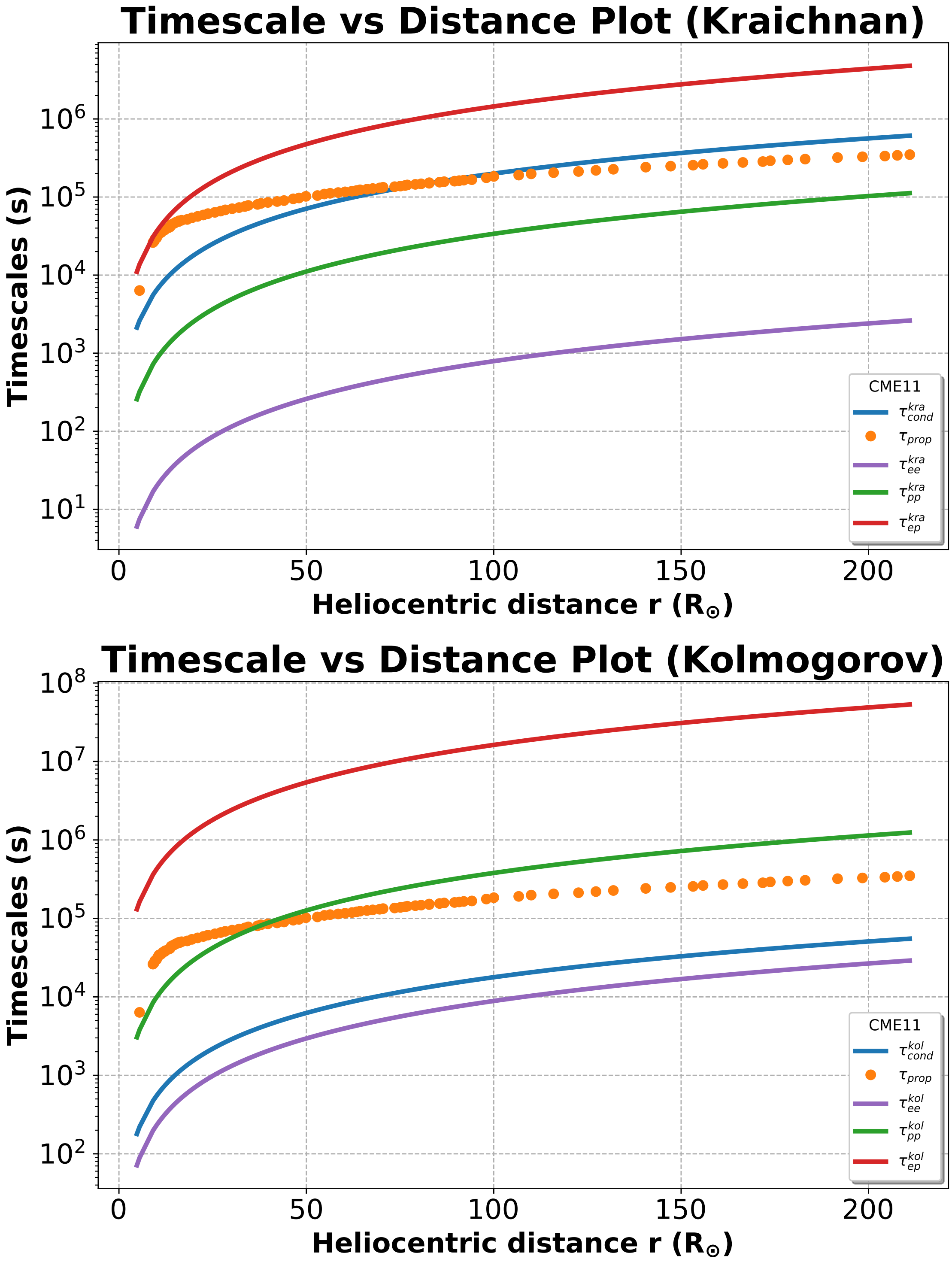

Figure 5.3: Non-Spitzer Timescales vs Distance Plots for CME11

For Spitzer case, we can see from Figure 5.1 that the electron conduction timescale τ_{cond} is about 5 orders of magnitude smaller than the CME propagation time τ_{prop} near the Sun, and it becomes 3 orders of magnitude smaller as it approaches near Earth. The collisional timescales (τ_{ee}, τ_{pp} and τ_{ep}) are even larger than τ_{cond} by $6 - 8$ orders of magnitude. Therefore, thermal conduction is quite faster than CME propagation.

However, for the anomalous/non-Spitzer case (Figures 5.2 and 5.3), the results depend on the turbulence model used.

1. **Kraichnan turbulence:** The electron conduction timescale τ_{cond} modified by Kraichnan turbulence is approximately equal to the propagation time τ_{prop}. It is greater than τ_{ee} and τ_{pp}, but less than τ_{ep}.

2. **Kolmogorov Turbulence:** For Kolmogorov turbulence, τ_{cond} is less than τ_{prop}, τ_{pp} and τ_{ep}, but greater than τ_{ee}.

The reason why the anomalous collisional timescales decrease by several orders of magnitude relative to the Spitzer case is because the magnetic field fluctuations act as scattering centers for the electrons to collide, effectively reducing the mean free path of collisions.

Another trend is that all three Kolmogorov collision timescales are larger than the Kraichnan timescales by a factor of 10. In other words, turbulent suppression of thermal conductivity is more pronounced for Kraichnan turbulence, as compared to Kolmogorov turbulence. Hence, we can infer that electron thermal conduction in a CME is faster for Kolmogorov turbulence than Kraichnan turbulence.

5.2 Velocity vs Distance Plots

Plotted below are the CME velocity profiles (Equation 4.1) superposed with the velocity of thermal conduction fronts (Equations 3.14 and 3.21).

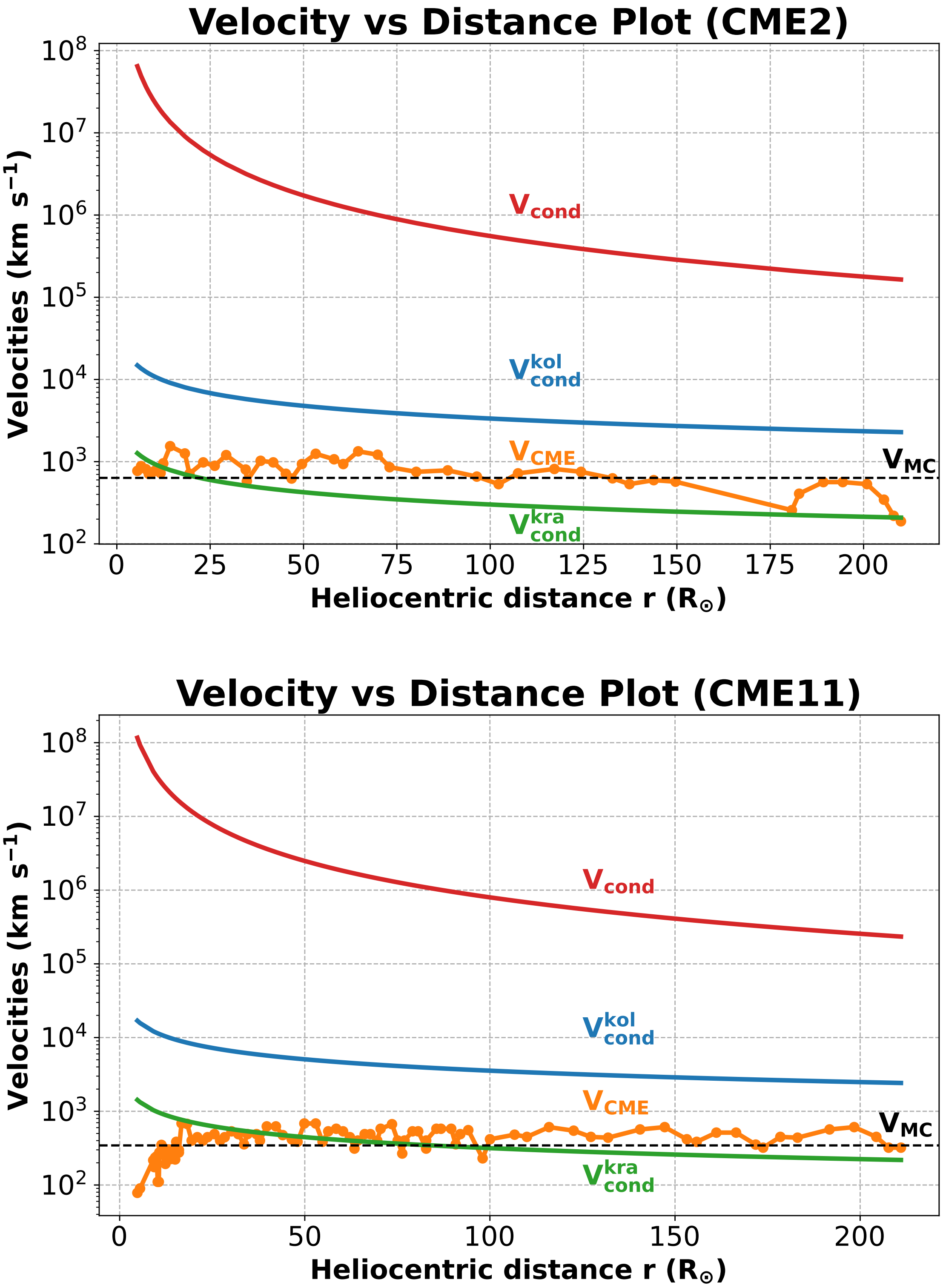

Figure 5.4: Velocity Profiles for CME2 and CME11

In order to understand these results better, let us revisit how electrons travel within an ICME. As we have seen in Figure 1.3, ICMEs carry a stream of bi-directional electrons (BDEs). This counter-streaming suprathermal electron population has been detected via in situ spacecrafts. Their existence emphasizes the assumption that both legs of the ICME flux rope are connected to the Sun throughout its propagation. The electron thermal conductivity is then along the direction of the magnetic field $\mathbf{B}$. This is illustrated in Figure 5.5.

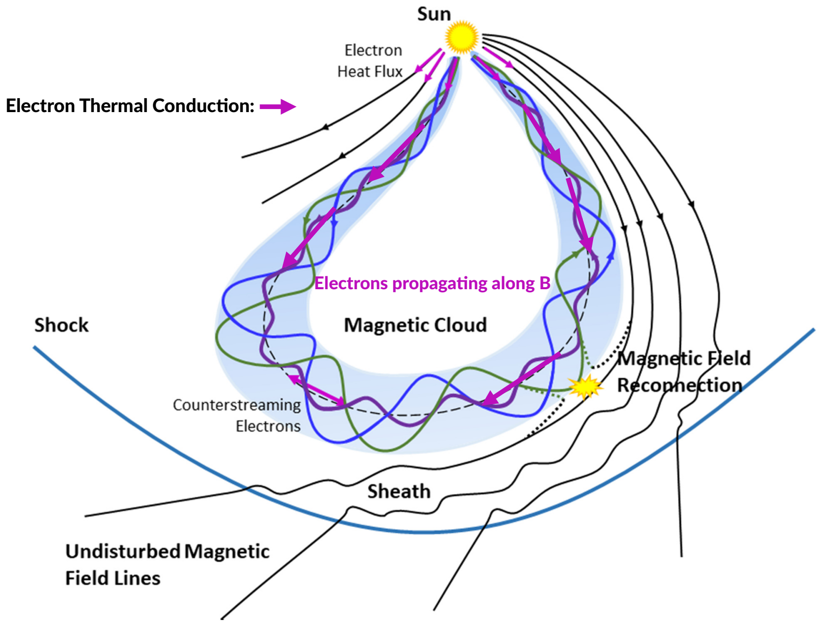
Sun
Electron Heat Flux
Electron Thermal Conduction:
Electrons propagating along B
Magnetic Cloud
Shock
Magnetic Field Reconnection
Counterstreaming Electrons
Sheath
Undisturbed Magnetic Field Lines

Figure 5.5: A cartoon of ICME showing the direction of electron propagation and heat flux. This image is modified from Wang et al. (2010) [8].

The thermal conduction front velocities for Spitzer and non-Spitzer conductivity are calculated using the expressions given in Equations 3.14 and 3.21. V_{CME} is estimated from Equation 4.1 using the method described in the previous chapter. V_{MC} is the average in situ CME velocity at the WIND frame of reference ($\approx 213\,\mathrm{R}_{\odot}$). These velocities are shown with appropriate labels in Figure 5.4.

5.2.1 Spitzer Case

From Figure 5.4, it can be seen that the thermal conduction front is about $10^5 - 10^3$ times faster than a typical CME. This observation is consistent with the previous results obtained from the timescale profiles.

5.2.2 Kraichnan Case

Here, the conduction front velocity (V_{cond}) is comparable to the CME velocity (V_{CME}), with V_{cond} being generally faster than V_{CME} near-Sun. The CME overtakes the conduction front at later distances. As we discussed in the previous section, Kraichnan turbulence increases the suppression of thermal conduction, and hence we get these comparable velocities.

5.2.3 Kolmogorov Case

The conduction front velocity is approximately 10 times higher than the CME propagation velocity for all of the events in this case. We had already established in the previous section that the Kolmogorov conduction timescale is a factor of 10 lower than the Kraichnan conduction timescale. The velocities reflect the same results; i.e. electron thermal conduction front is faster for Kolmogorov turbulence-modified conductivity than a propagating CME.

Now let us try to understand the observed velocity profiles. The conduction front velocities (V_{cond}) are essentially the propagation speed of a representative thermal packet. Say both the thermal packet and the CME start out from the Sun at the same time. We are simply asking: which one of the two is faster than the other? In order for conduction to be efficient, the thermal packet will have to catch up with the CME. If it cannot catch up, then thermal conduction is just not fast enough. This race between the conduction front and CME yields different winners for the Spitzer and Non-Spitzer scenarios. The three different cases of our results are visualised in the following Figure 5.6.

1. For Spitzer thermal conduction, the thermal packet has overtaken the CME by a significant distance. Therefore, conduction is very efficient, and heat is readily flowing from the solar corona to the interior of the CME.
2. In the case of Kolmogorov turbulence, the thermal packet is still way ahead of the CME leading edge throughout their propagation, and hence we could say that heat is efficiently being transported.
3. For Kraichnan turbulence, the thermal packet is faster than the CME initially, but the CME overtakes the conduction front later on. The two speeds remain comparable, with the CME leading edge being slightly faster.

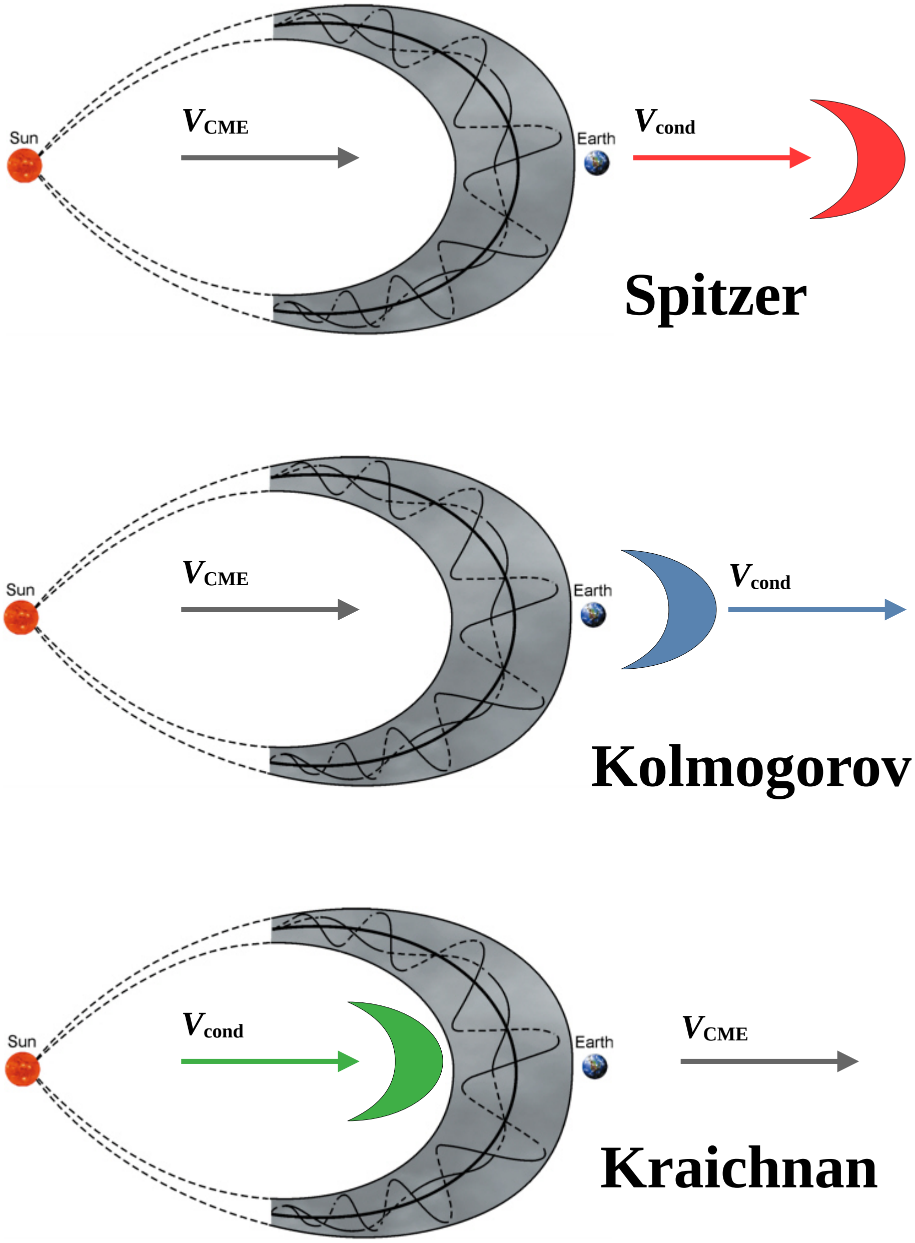
Sun
V_{CME}
Earth
V_{cond}
Spitzer
Sun
V_{CME}
Earth
V_{cond}
Kolmogorov
Sun
V_{cond}
Earth
V_{CME}
Kraichnan

Figure 5.6: A comparison between three different conduction scenarios.

5.3 Proton Heating through Thermal Equilibration

From the results in the previous two sections, we can see that electrons seem to be thermally connected to the corona for both Spitzer and Kolmogorov cases. However, this does not imply anything concrete about proton energetics. From the timescale plots (Figures 5.1 – 5.3), it is evident that τ_{pp} is almost 50 times higher than τ_{ee}. Proton thermal conductivity is also about 10^3 times smaller than electron thermal conductivity, owing to their heavier mass and less mobility.

Since protons are observed to have temperatures $\approx 10^5\,\mathrm{K}$, we ask what is the rate of the energy transfer from electrons to protons through thermal equilibration.

The heating rate $(\mathrm{erg\,s^{-1}})$ due to thermal equilibration via Coulomb collisions between electrons and protons is given as (Liu et al., Eilek and Kafatos (2006, 1983) [35, 45]):

$$H = \frac{k_{\mathrm{B}}\,(T_e - T_p)}{\tau_{ep}} \tag{5.1}$$

where τ_{ep} is the electron-proton collision timescale. The heating rate is calculated for Spitzer, Kraichnan and Kolmogorov cases and plotted against r for CME2 and CME11 as shown below.

For reference, Štverák et al. (2015) [46] have computed the heating rate per number density as a function of heliocentric distance due to Coulomb electron-proton collisions in the fast and slow solar wind. They found the value to be very negligible owing to very low frequency of the electron-proton collisions.

As we can see from Figure 7.20, the heating rate associated with thermal equilibration via electron-proton collisions is quite small $(< 10^{-12}\,\mathrm{erg\,s^{-1}})$ for the three cases. For purely Spitzer case, our values seem to be in agreement with the findings of Štverák et al. (2015) for solar wind.

Therefore, we could say that electron-proton equilibration is not efficient in explaining proton heating in CMEs for Spitzer collisions, and thus we require additional sources to explain the high proton temperature in the CME plasma.

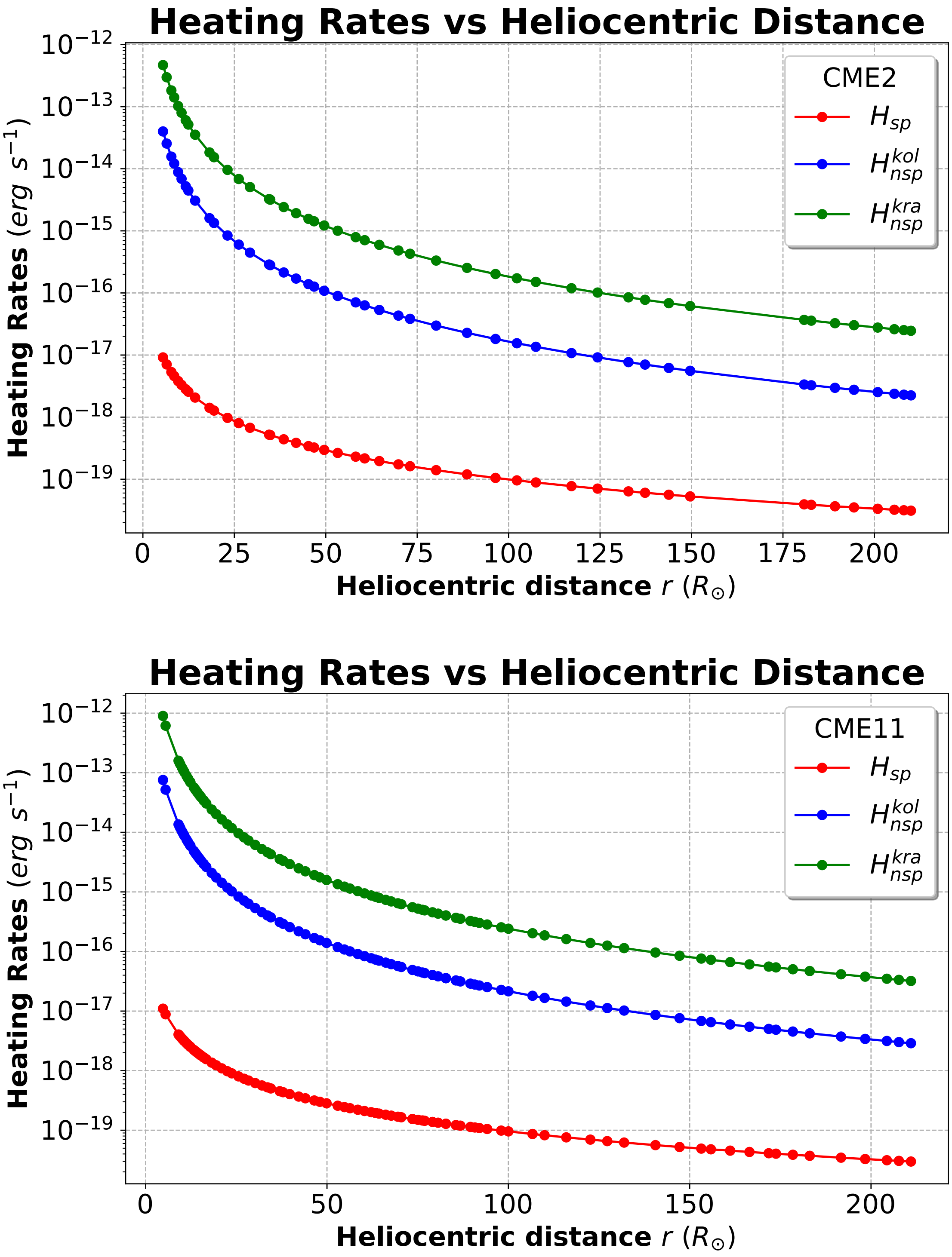

Figure 5.7: Heating Rate vs Distance Plots for CME2 and CME11

Chapter 6

Conclusions and Future Work

6.1 Electron Thermal Conduction

6.1.1 Spitzer Case

For all of the observed CMEs, electron thermal conduction front velocity V_{cond} is found to be much faster than the corresponding Sun-Earth propagation velocity $V_{\rm CME}$. This implies that thermal conduction in CMEs is efficient, and thus heat will readily flow from the solar corona to the interior of the ICME. This could support the use of the isothermal value of $\gamma \approx 1$ in CME propagation models.

6.1.2 Anomalous or Non-Spitzer Case

Since the plasma in the ambient solar wind as well as the CME interior is nearly collisionless, conventional estimates of plasma heating or thermal conductivity based on Spitzer-Coulomb collisions may not be valid. Turbulence-mediated Coulomb collisions affected by magnetic field fluctuations will give a more realistic estimate. These turbulent fluctuations lead to a suppression of thermal conductivity. Our results confirm this suppression.

1. Assuming Kraichnan turbulence, V_{cond} reduces by over 3 orders of magnitude from the Spitzer

values, such that it now has similar values as $V_{\rm CME}$. Although the conduction front is faster initially, it lags behind the CME at later distances.

2. However, V_{cond} is higher than $V_{\rm CME}$, assuming Kolmogorov turbulence. Therefore thermal conduction along the magnetic fields is quite effective.

Using multi-spacecraft surveys, Liu et al. (2006) [35] have performed a statistical study of ICMEs to understand their heating mechanisms. They found that the observed power spectrum for magnetic field fluctuations within an ICME plasma follows Kolmogorov scaling. Our findings on Kolmogorov turbulence-modified conductivity are in agreement with these results, and this suggests that CME expansion is nearly isothermal, and the corresponding polytropic index γ will be close to one.

6.2 Proton Heating Rates

While our preliminary results seem to suggest that electrons are thermally well connected to the corona, it is not clear if this has a bearing on proton energetics. Electron-proton equilibration is a slow process and the transfer of energy from electrons to protons is expected to be quite inefficient. We have estimated the heating rate of electron-proton thermal equilibration as a function of r for the same set of 38 CMEs throughout their propagation. We find that the values are pretty low for both Spitzer and non-Spitzer cases. There is thus a need for additional proton heating, and turbulent dissipation on protons might be an answer.

6.3 Future Work

As we have come to the end of this thesis, we now outline a potential plan for further investigation of plasma heating inside CMEs.

1. We have compared CME leading front velocities with thermal conduction front velocities. While the thermal conduction front seems to travel faster than the CME in the outer corona and heliosphere, it seems that this is not uniformly true in the inner corona – especially for fast CMEs. Such comparisons are complicated by the sparse availability of Sun-Earth

tracking data for CMEs. Nevertheless, there are some CMEs that have been well-tracked in the inner corona (e.g., Gou et al., Cheng et al., Joshi and Srivastava, Majumdar et al. (2019, 2020, 2011, 2020) [47–50]). It may be possible to draw more concrete inferences regarding this comparison in the inner corona. There are several challenges, such as the availability of height-time or velocity-height data (the data will likely have to be digitized), and the choice of an appropriate density and temperature model to use.

2. As we (and several others) have remarked, the necessity for proton heating can be motivated by recognizing that protons in an adiabatically expanding parcel of solar wind will cool down to a few kelvins by the time it reaches the Earth. However, this is a rather general statement – it is based on inferred expansion profiles for the ambient solar wind, which may not hold for CMEs. CME expansion has been well characterized (e.g., Sachdeva et al., Bothmer and Schwenn (2017, 1998) [1, 51]) and used for inferring CME thermodynamics (Mishra and Wang, Wang et al. (2018, 2009) [23, 52]) We can use the observed CME self-similar expansion characteristics to deduce the required proton heating rate inside CMEs using Equations 9-11 of Vasquez et al. (2007) [16], which is derived by Verma et al. (1995) [15]. Such a calculation will be CME-specific, and not merely use solar wind expansion rates. The answers are likely to be different.

3. It is also worth looking at alternative electron-proton equilibration mechanisms and the resulting thermal conductivity - e.g., section 4.3 of Laming (2004) [53], especially in comparison with the turbulence-modified conduction rates we propose.

Chapter 7

Appendix

7.1 Table of Physical Constants and Plasma Parameters

Table 7.1: Numerical values of physical constants and plasma parameters used in this thesis. This table is made using Appendices A and D of *Physics of the Solar Corona* by Aschwanden (2005) [3].

Physical Quantity	**Expression**	**Numerical Formula**	**CGS Units**
Speed of light in vacuum	c	2.9979×10^{10}	$\mathrm{cm\,s^{-1}}$
Elementary charge	e	4.8032×10^{-10}	statcoulomb/e.s.u.
Electron mass	m_e	9.1094×10^{-28}	g
Proton mass	m_p	1.6726×10^{-24}	g
Proton/electron mass ratio	m_p/m_e	1.8361×10^{3}	
Boltzmann constant	k_{B}	1.3807×10^{-16}	$\mathrm{erg\,K^{-1}}$
Sun-Earth distance	1 AU	1.4959×10^{13}	cm
Solar radius	$1\ \mathrm{R}_{\odot}$	6.957×10^{10}	cm
Electron thermal velocity	$v_{T_e} = (k_{\mathrm{B}} T_e/m_e)^{1/2}$	$3.89 \times 10^{5}\, T_e^{1/2}$	$\mathrm{cm\,s^{-1}}$
Proton thermal velocity	$v_{T_p} = (k_{\mathrm{B}} T_p/m_p)^{1/2}$	$9.09 \times 10^{3}\, T_p^{1/2}$	$\mathrm{cm\,s^{-1}}$
Electron gyrofrequency	$\omega_{ge} = eB/m_e c$	$1.76 \times 10^{7}\, B$	$\mathrm{rad\,s^{-1}}$
Proton gyrofrequency	$\omega_{gp} = eB/m_p c$	$9.58 \times 10^{3}\, B$	$\mathrm{rad\,s^{-1}}$
Electron gyroradius	$R_e = v_{T_e}/\omega_{ge}$	$2.21 \times 10^{-2}\, T_e^{1/2}\, B^{-1}$	cm
Proton gyroradius	$R_p = v_{T_p}/\omega_{gp}$	$9.49 \times 10^{-1}\, T_p^{1/2}\, B^{-1}$	cm
Coulomb logarithm	$\ln \Lambda$	20	

7.2 Timescale vs Distance Plots for the other CMEs

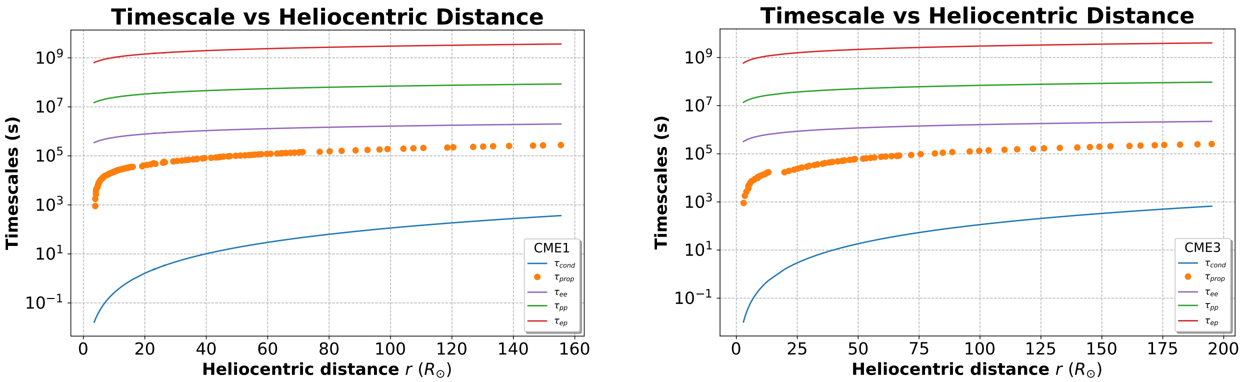

(a) Spitzer Timescales of CME1

(b) Spitzer Timescales of CME3

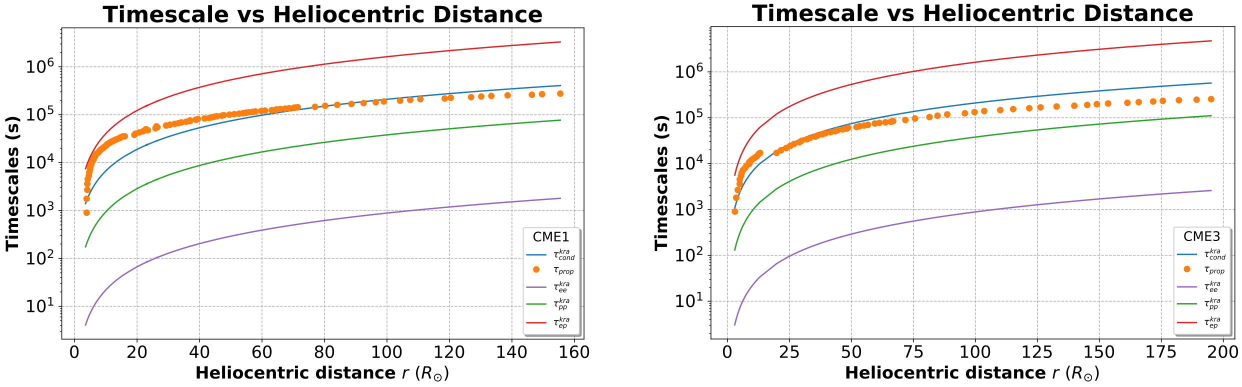

(c) Kraichnan Timescales of CME1

(d) Kraichnan Timescales of CME3

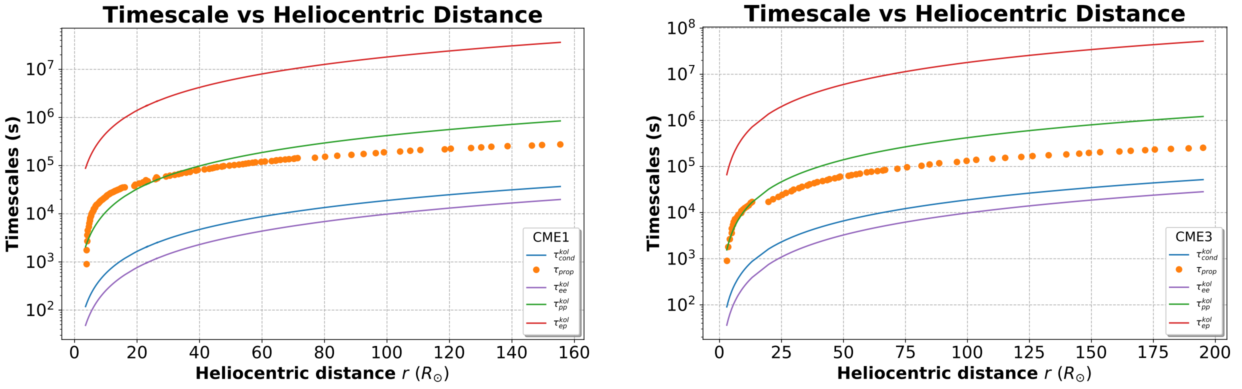

(e) Kolmogorov Timescales of CME1

(f) Kolmogorov Timescales of CME3

Figure 7.1: Timescale Profiles for CME1 & CME3

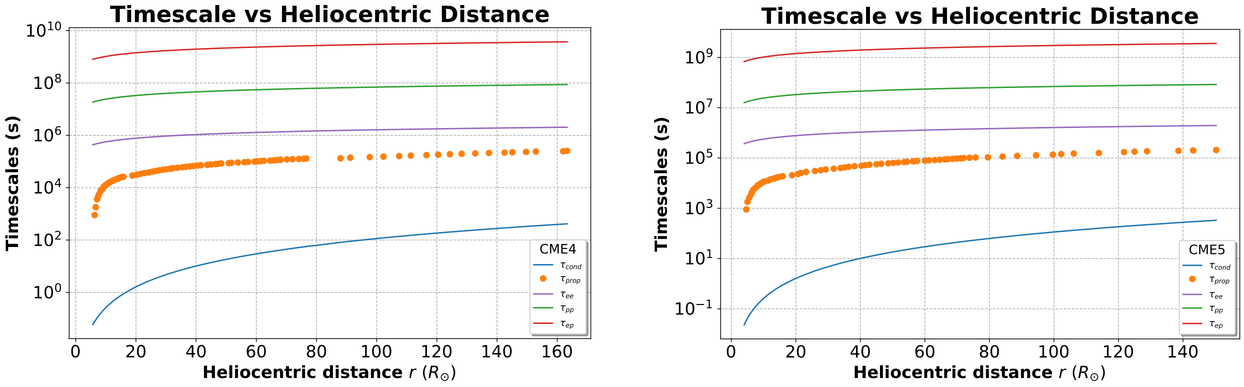

(a) Spitzer Timescales of CME4

(b) Spitzer Timescales of CME5

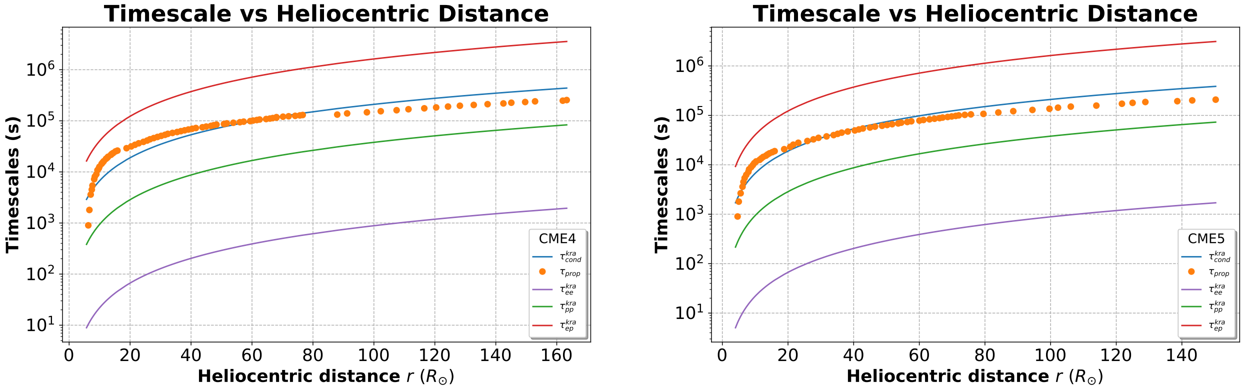

(c) Kraichnan Timescales of CME4

(d) Kraichnan Timescales of CME5

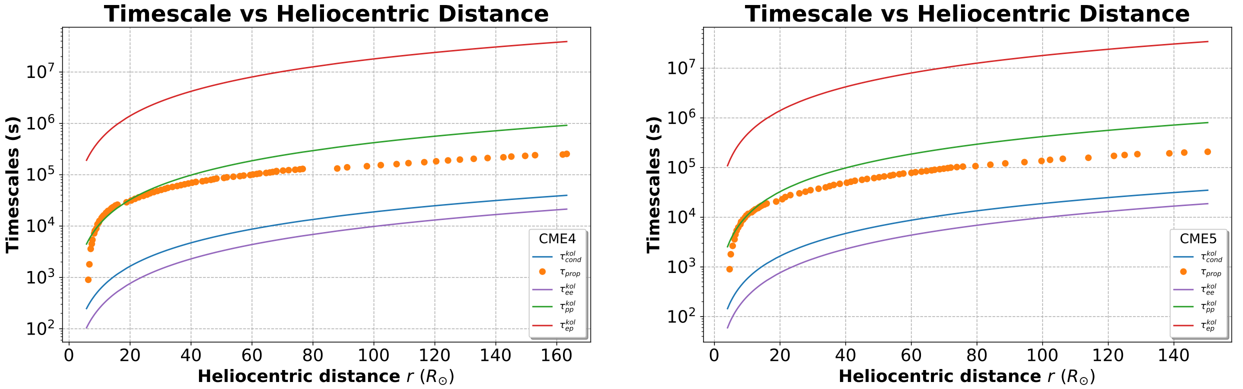

(e) Kolmogorov Timescales of CME4

(f) Kolmogorov Timescales of CME5

Figure 7.2: Timescale Profiles for CME4 & CME5

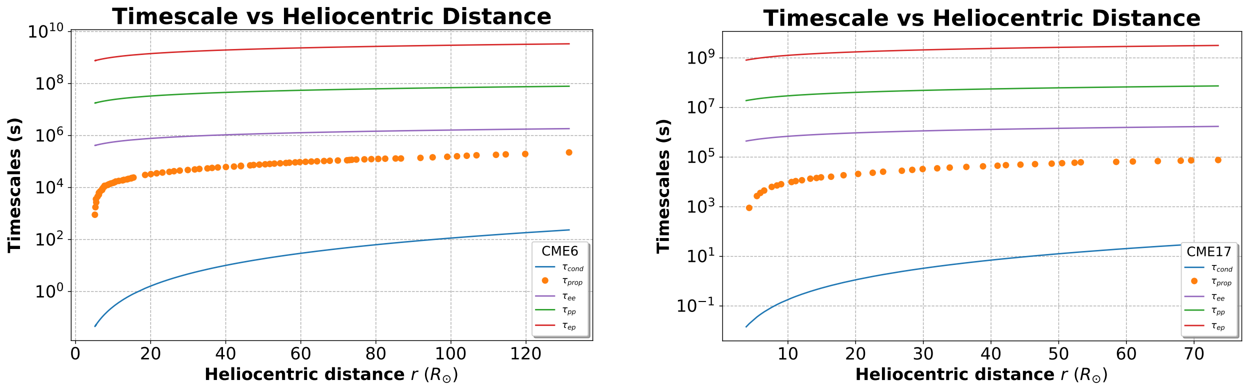

(a) Spitzer Timescales of CME6 **(b)** Spitzer Timescales of CME17

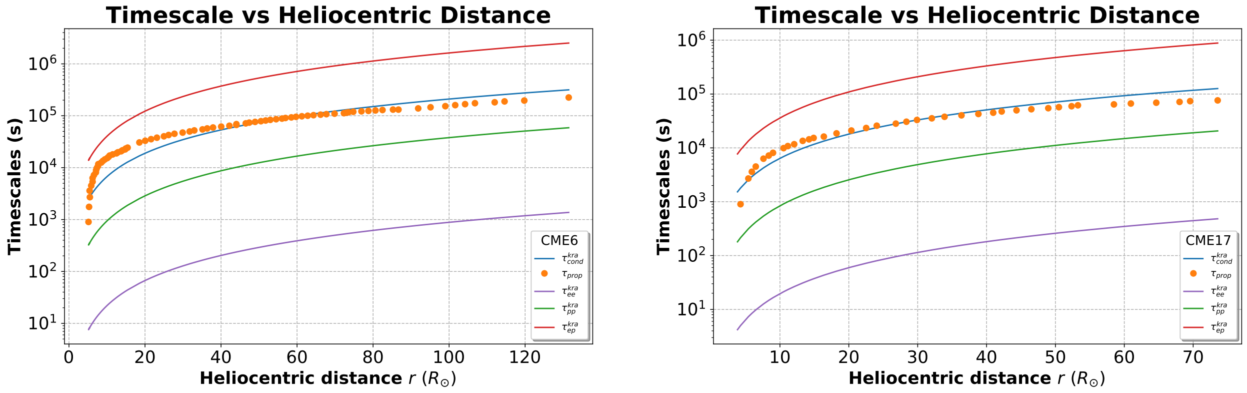

(c) Kraichnan Timescales of CME6 **(d)** Kraichnan Timescales of CME17

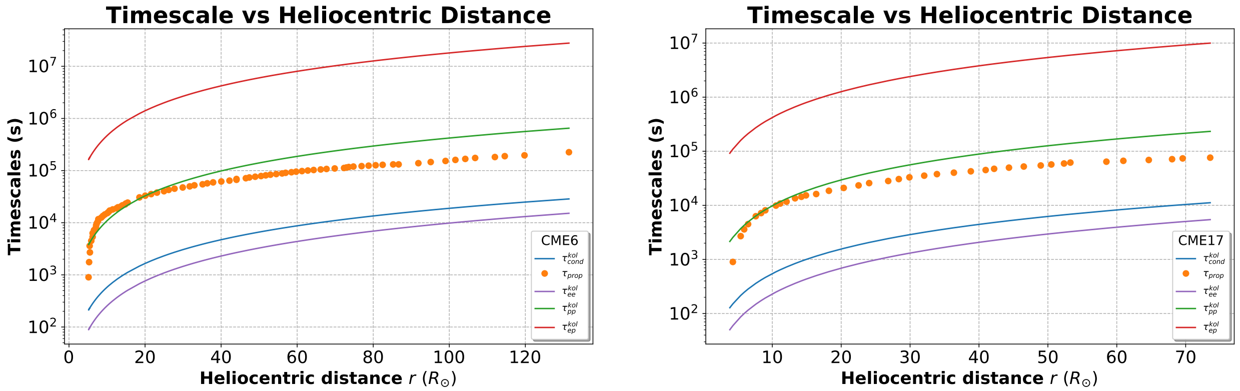

(e) Kolmogorov Timescales of CME6 **(f)** Kolmogorov Timescales of CME17

Figure 7.3: Timescale Profiles for CME6 & CME17

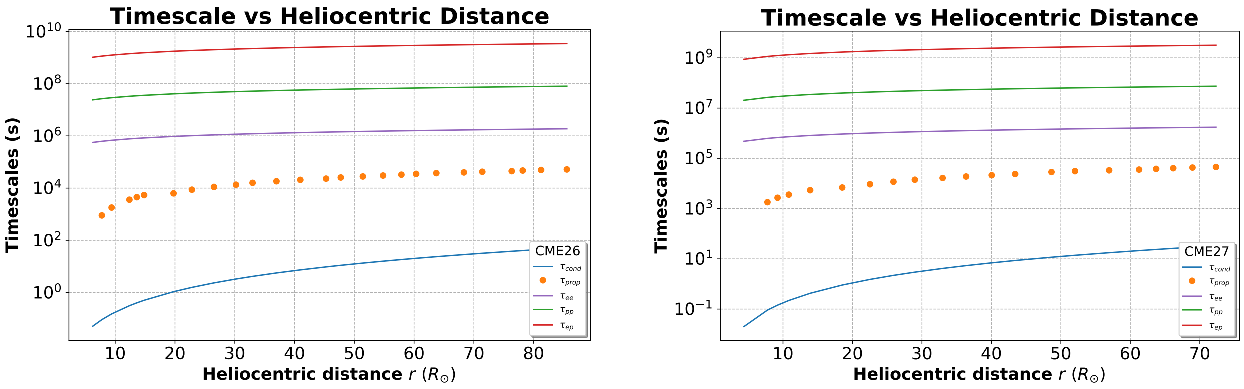

(a) Spitzer Timescales of CME26 **(b)** Spitzer Timescales of CME27

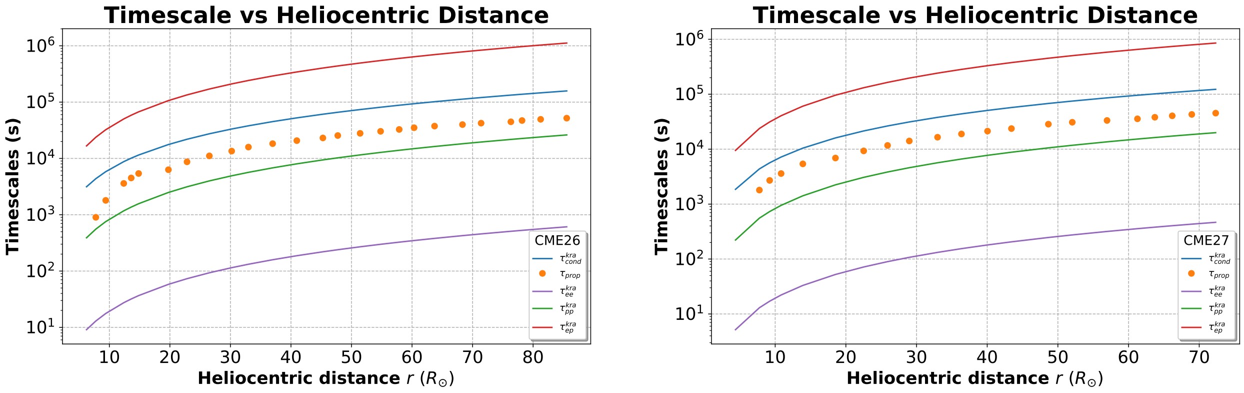

(c) Kraichnan Timescales of CME26 **(d)** Kraichnan Timescales of CME27

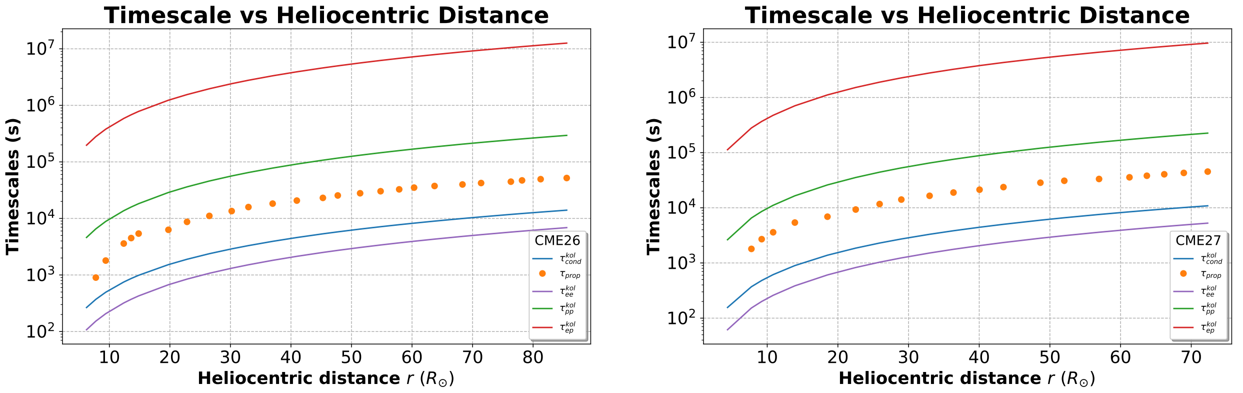

(e) Kolmogorov Timescales of CME26 **(f)** Kolmogorov Timescales of CME27

Figure 7.4: Timescale Profiles for CME26 & CME27

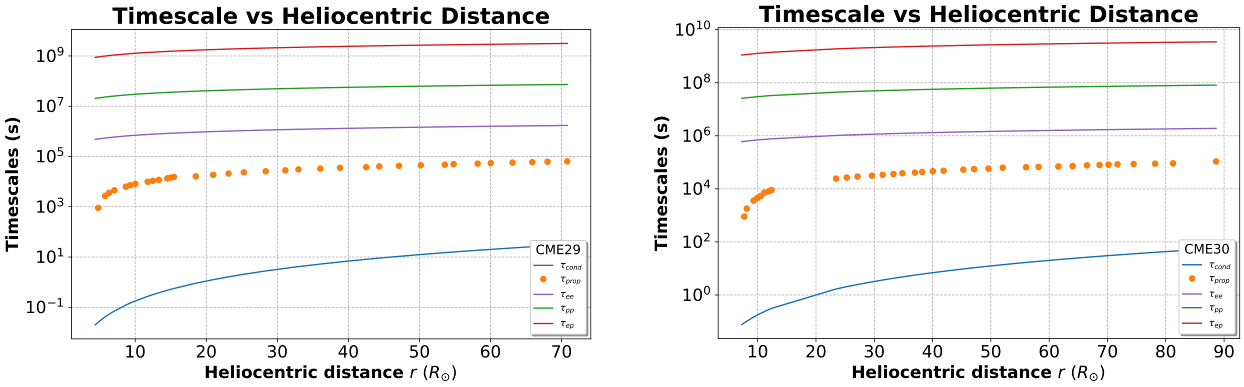

(a) Spitzer Timescales of CME29 **(b)** Spitzer Timescales of CME30

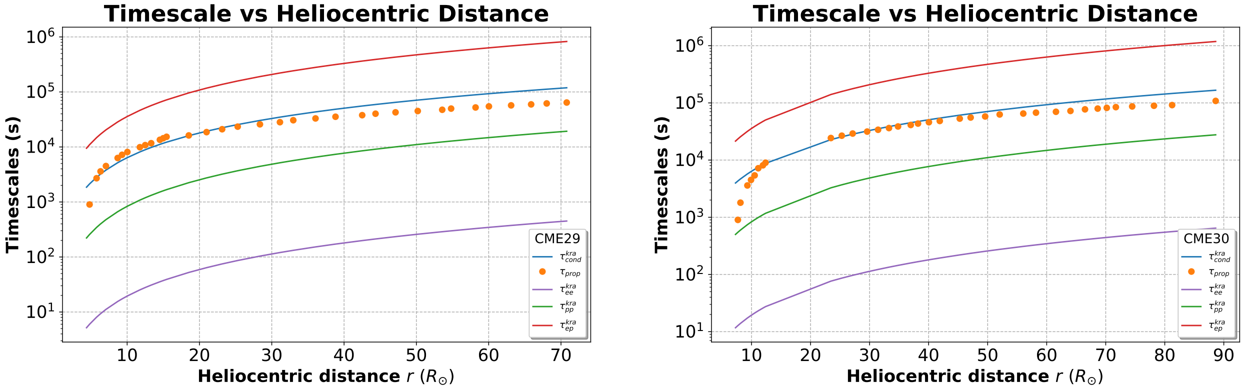

(c) Kraichnan Timescales of CME29 **(d)** Kraichnan Timescales of CME30

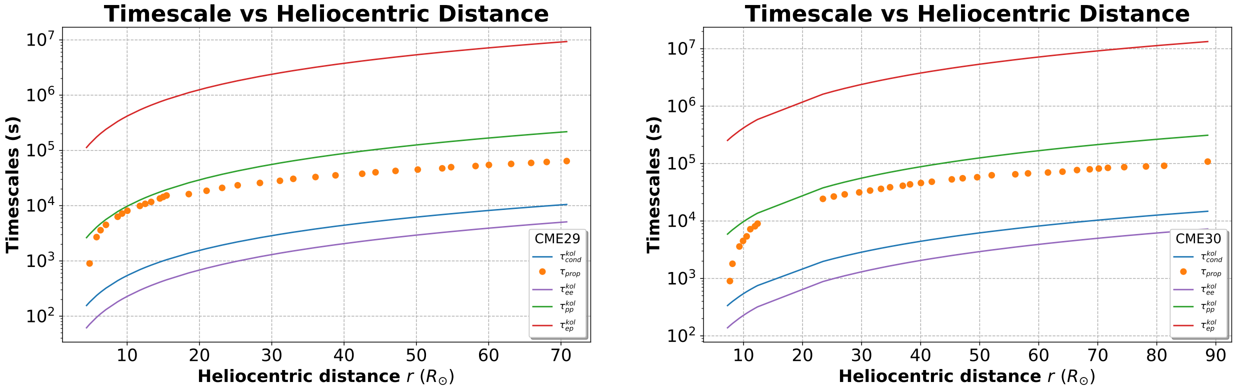

(e) Kolmogorov Timescales of CME29 **(f)** Kolmogorov Timescales of CME30

Figure 7.5: Timescale Profiles for CME29 & CME30

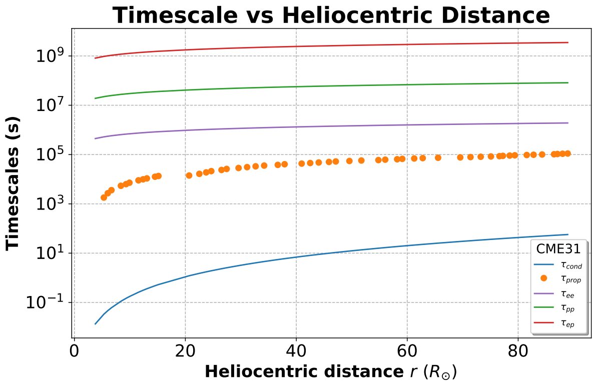

(a) Spitzer Timescales of CME31

(b) Spitzer Timescales of CME33

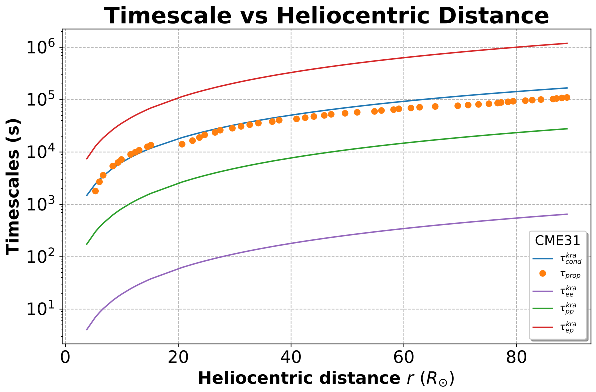

(c) Kraichnan Timescales of CME31

(d) Kraichnan Timescales of CME33

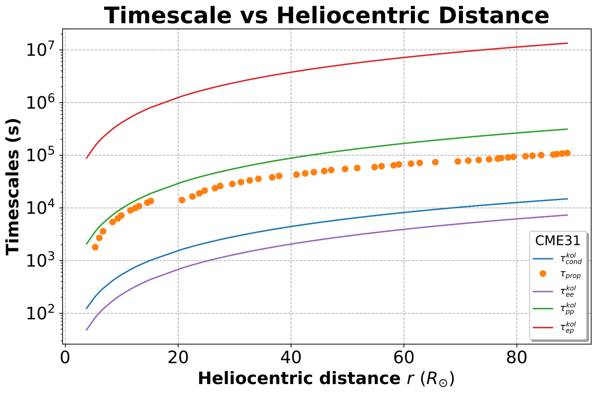

(e) Kolmogorov Timescales of CME31

(f) Kolmogorov Timescales of CME33

Figure 7.6: Timescale Profiles for CME31 & CME33

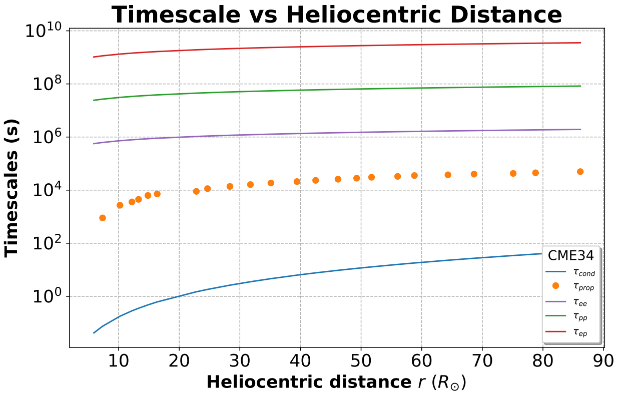

(a) Spitzer Timescales of CME34

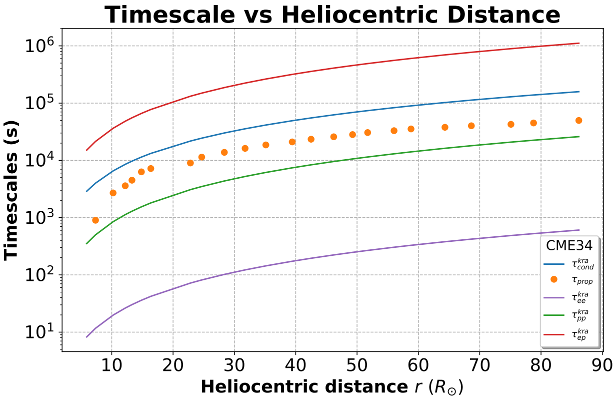

(b) Kraichnan Timescales of CME34

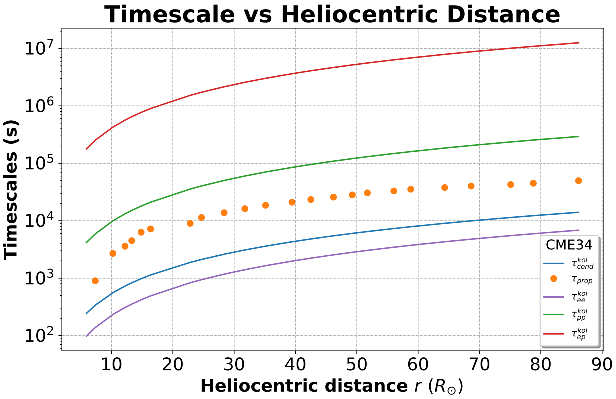

(c) Kolmogorov Timescales of CME34

Figure 7.7: Timescale Profiles for CME34

7.3 Velocity vs Distance Plots for the other CMEs

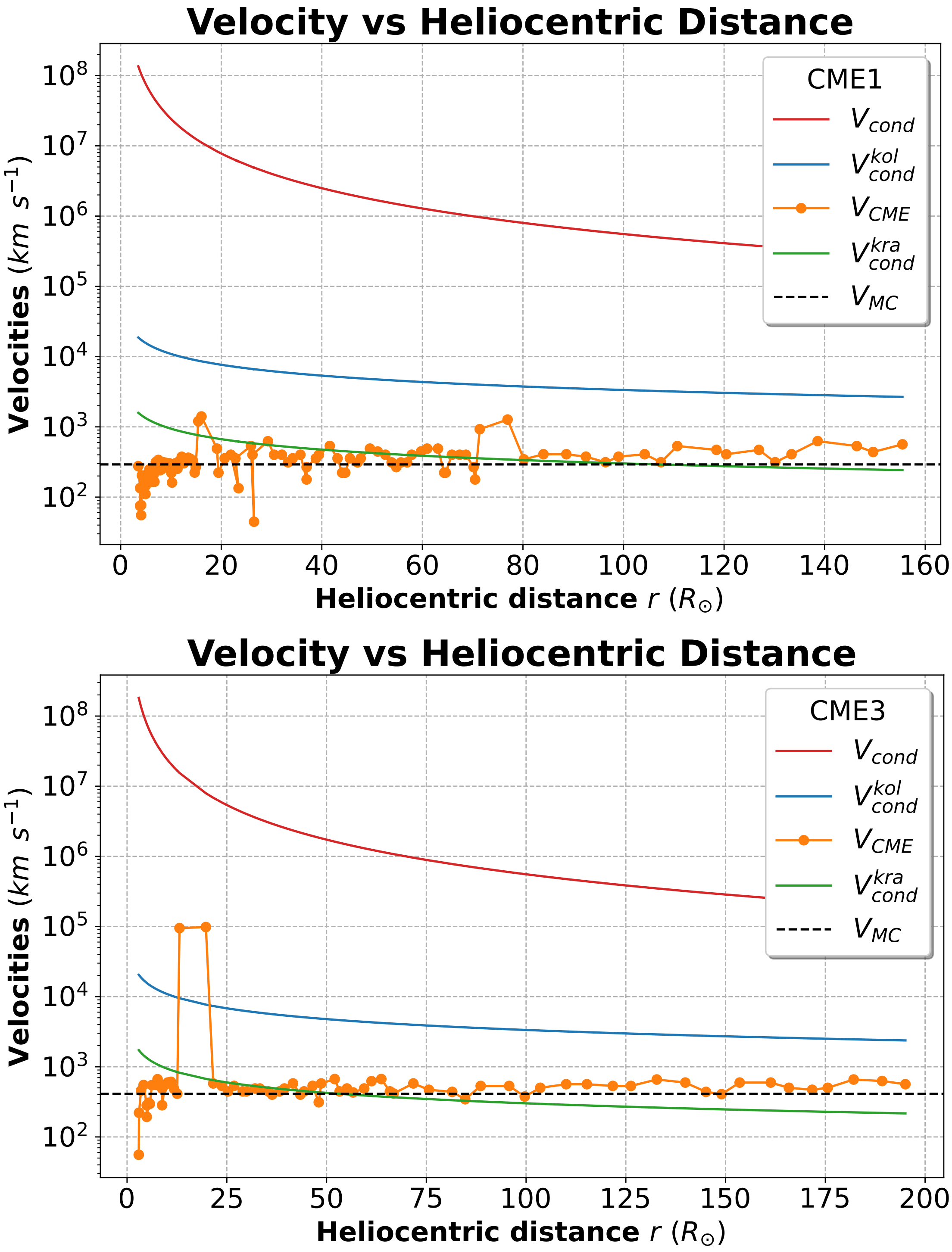

Figure 7.8: Velocity Profiles for CME1 & CME3

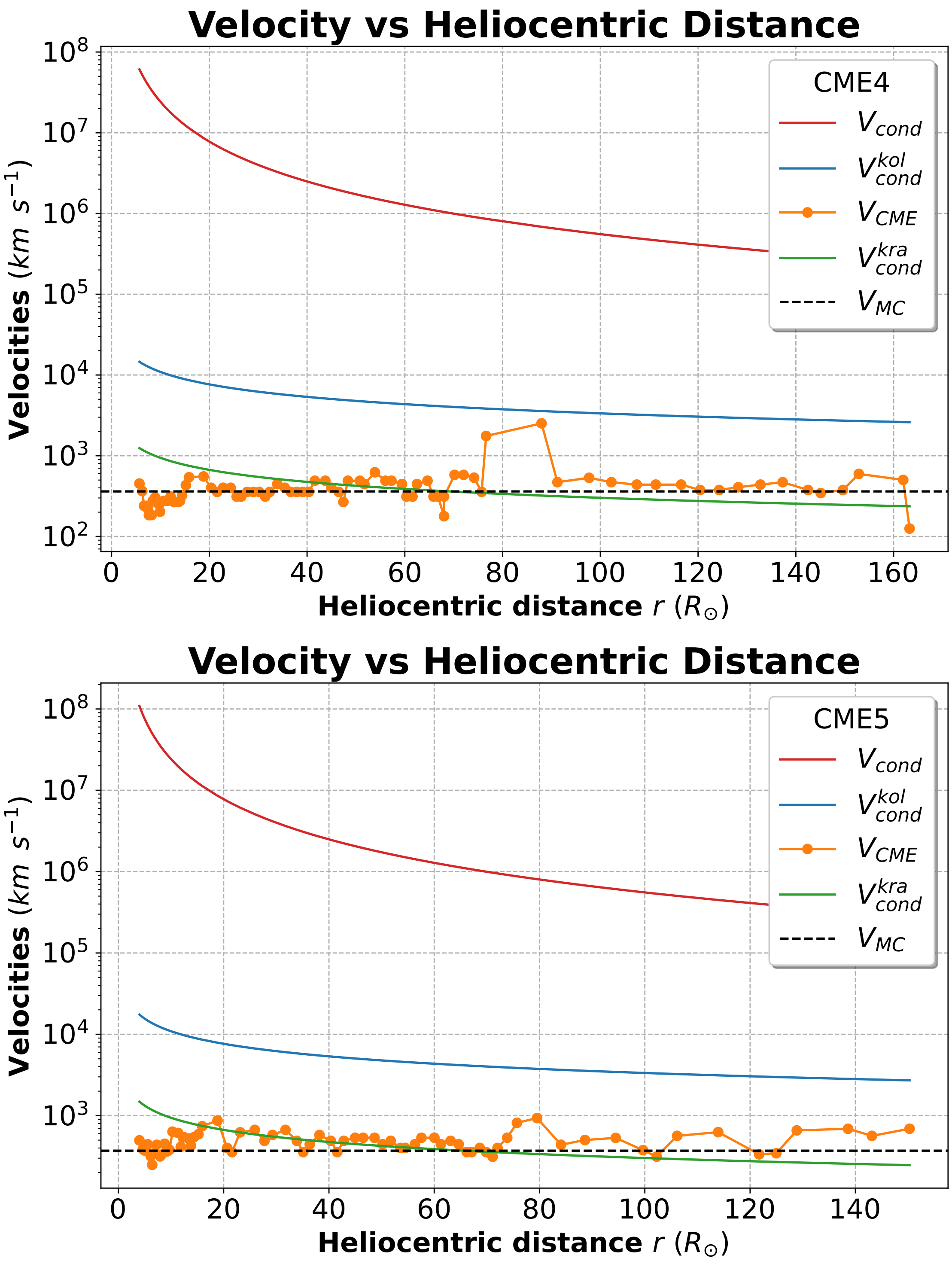

Figure 7.9: Velocity Profiles for CME4 & CME5

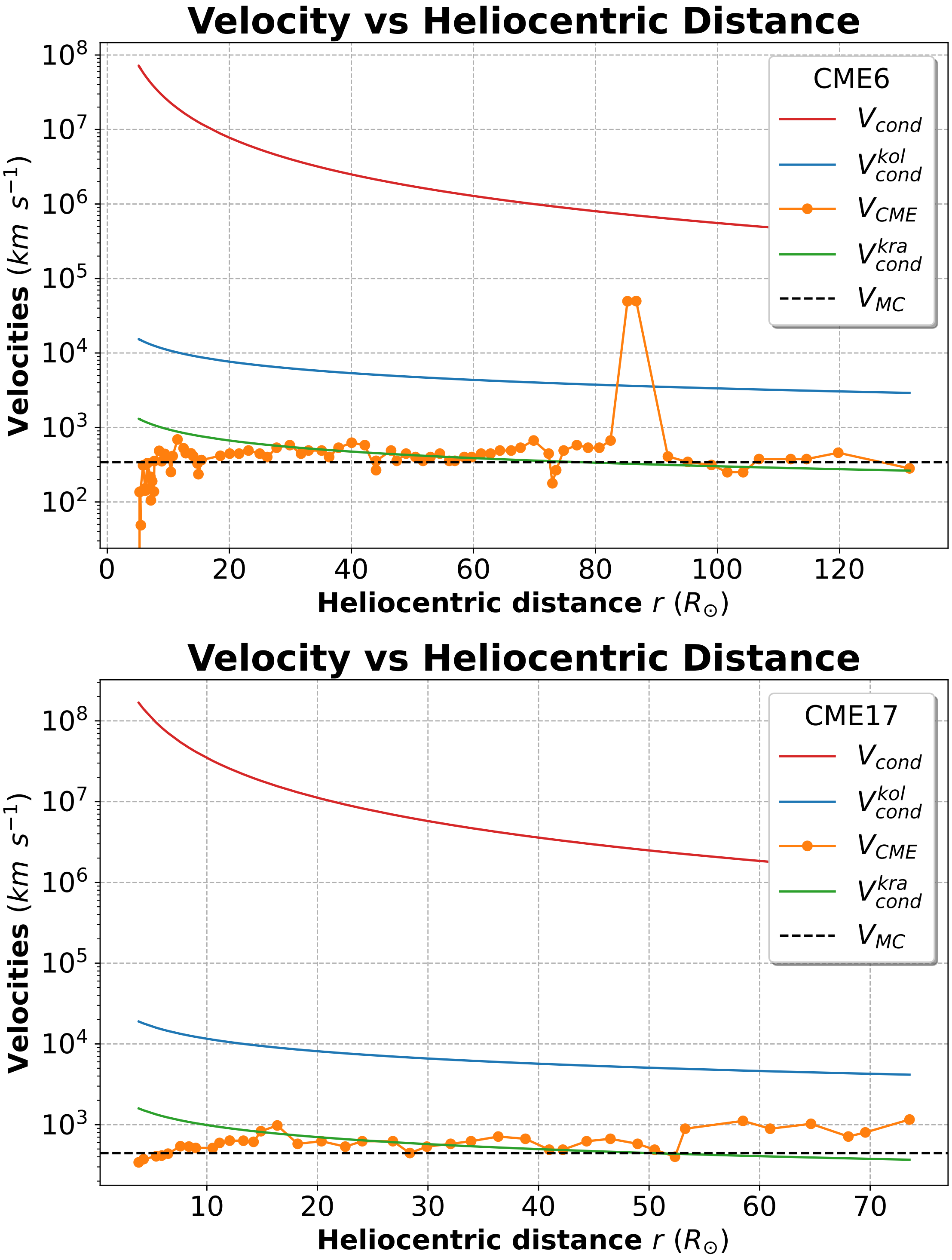

Figure 7.10: Velocity Profiles for CME6 & CME17

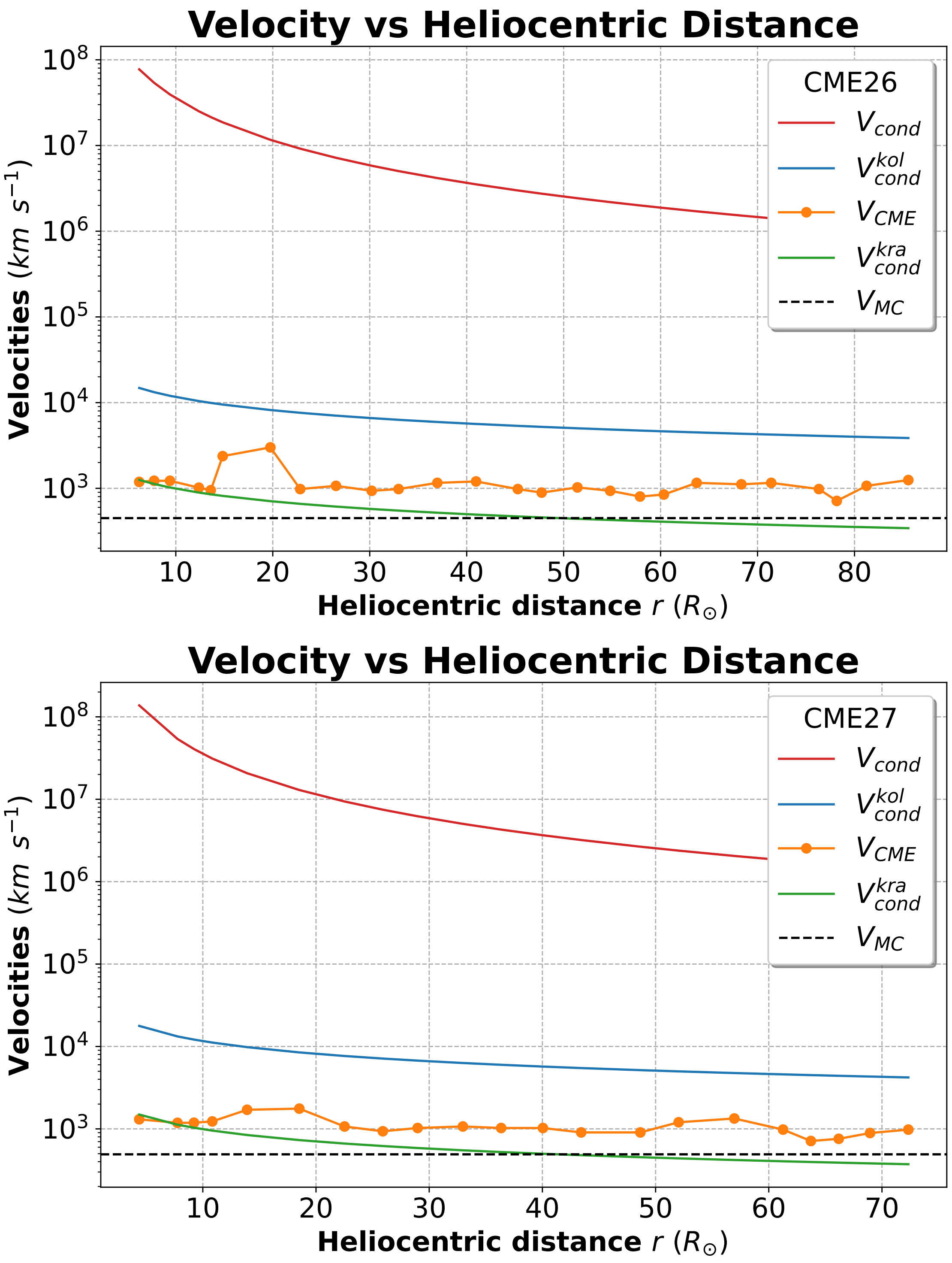

Figure 7.11: Velocity Profiles for CME26 & CME27

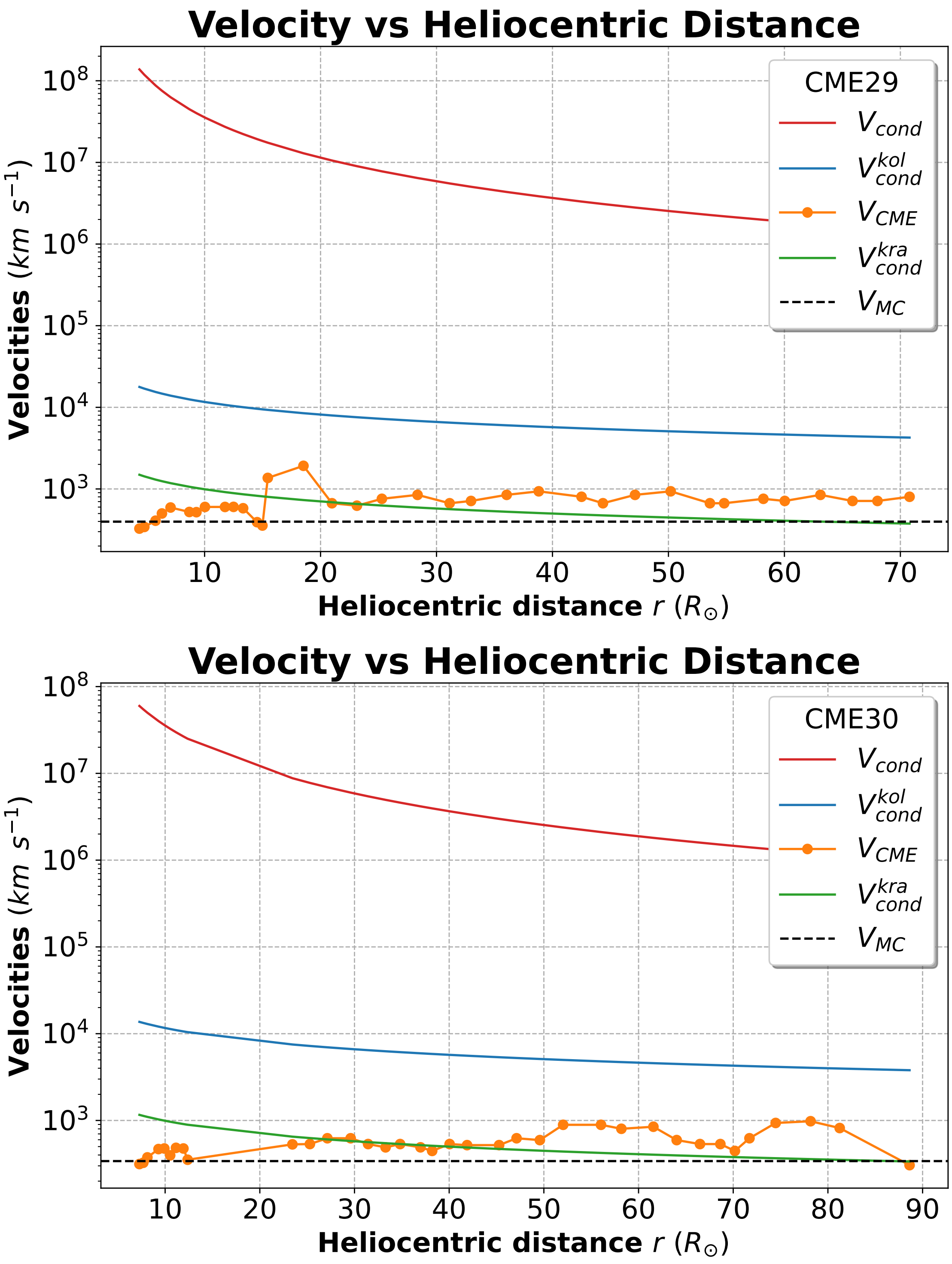

Figure 7.12: Velocity Profiles for CME29 & CME30

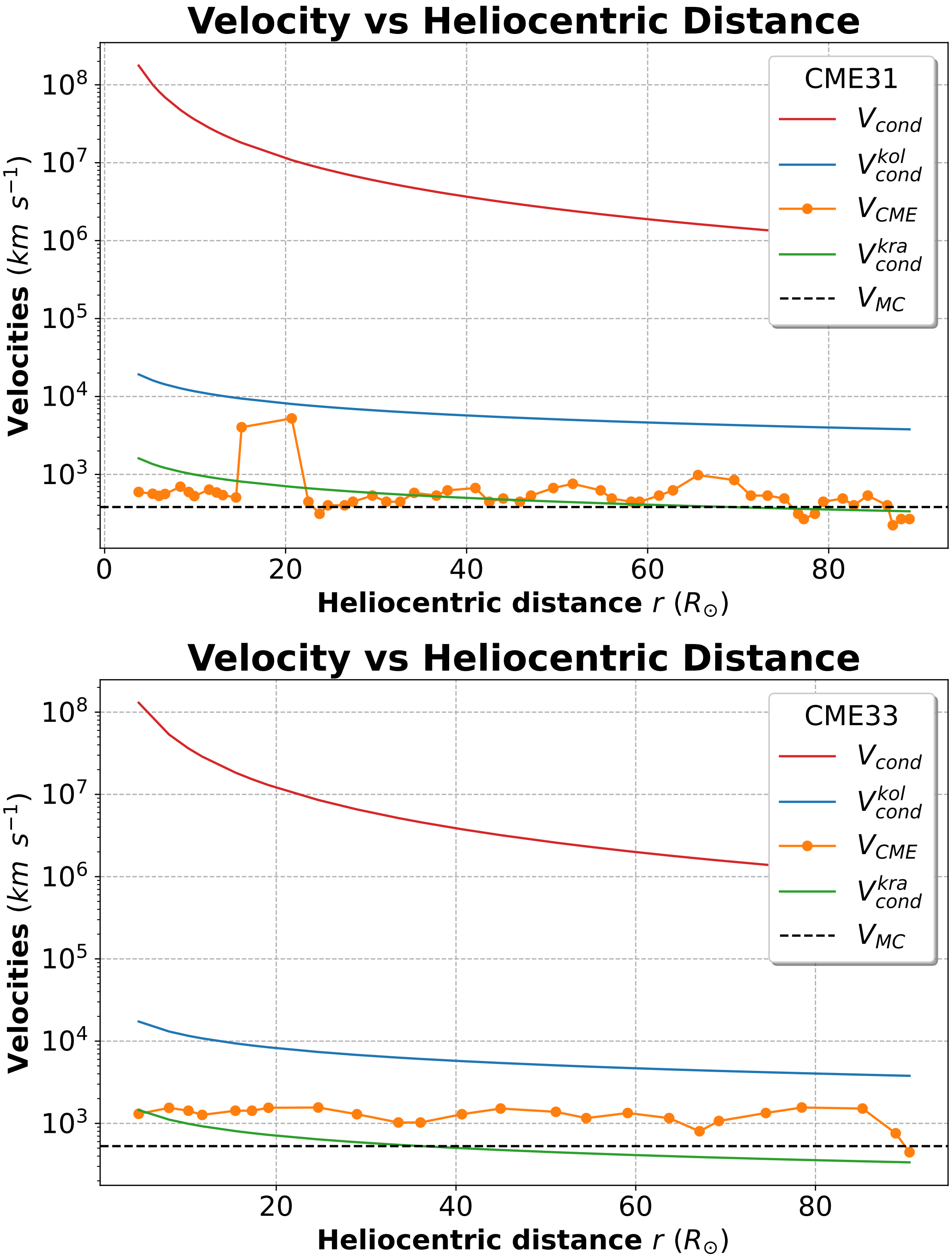

Figure 7.13: Velocity Profiles for CME31 & CME33

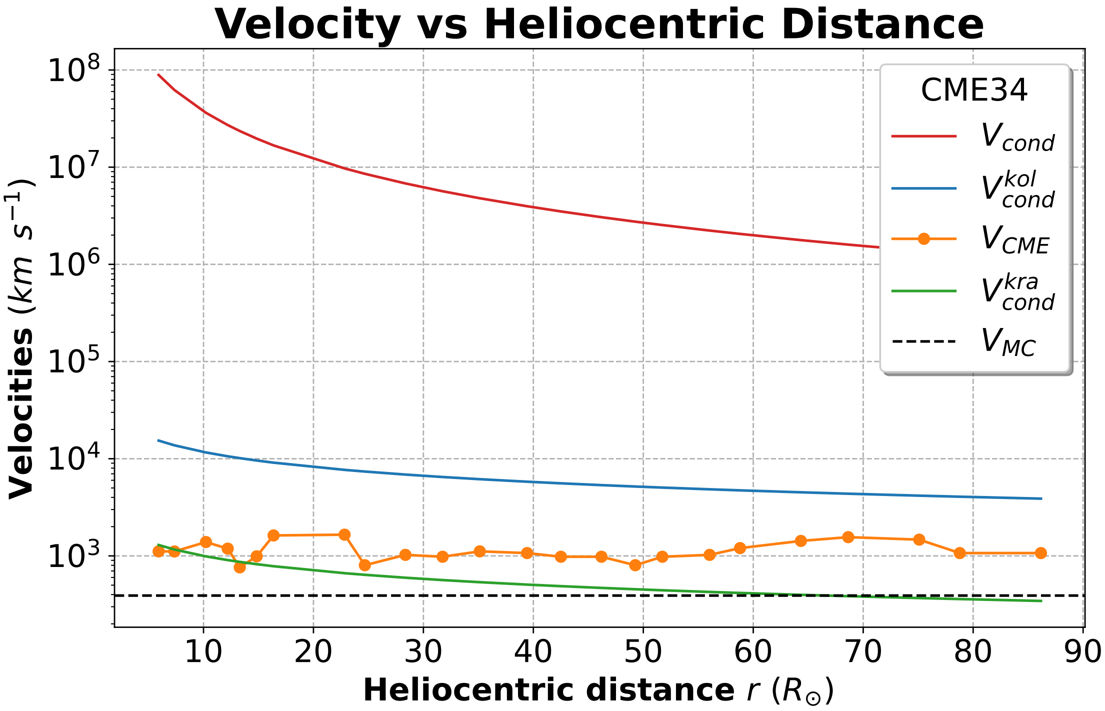

Figure 7.14: Velocity Profiles for CME34

7.4 Proton Heating Rate vs Distance Plots for the other CMEs

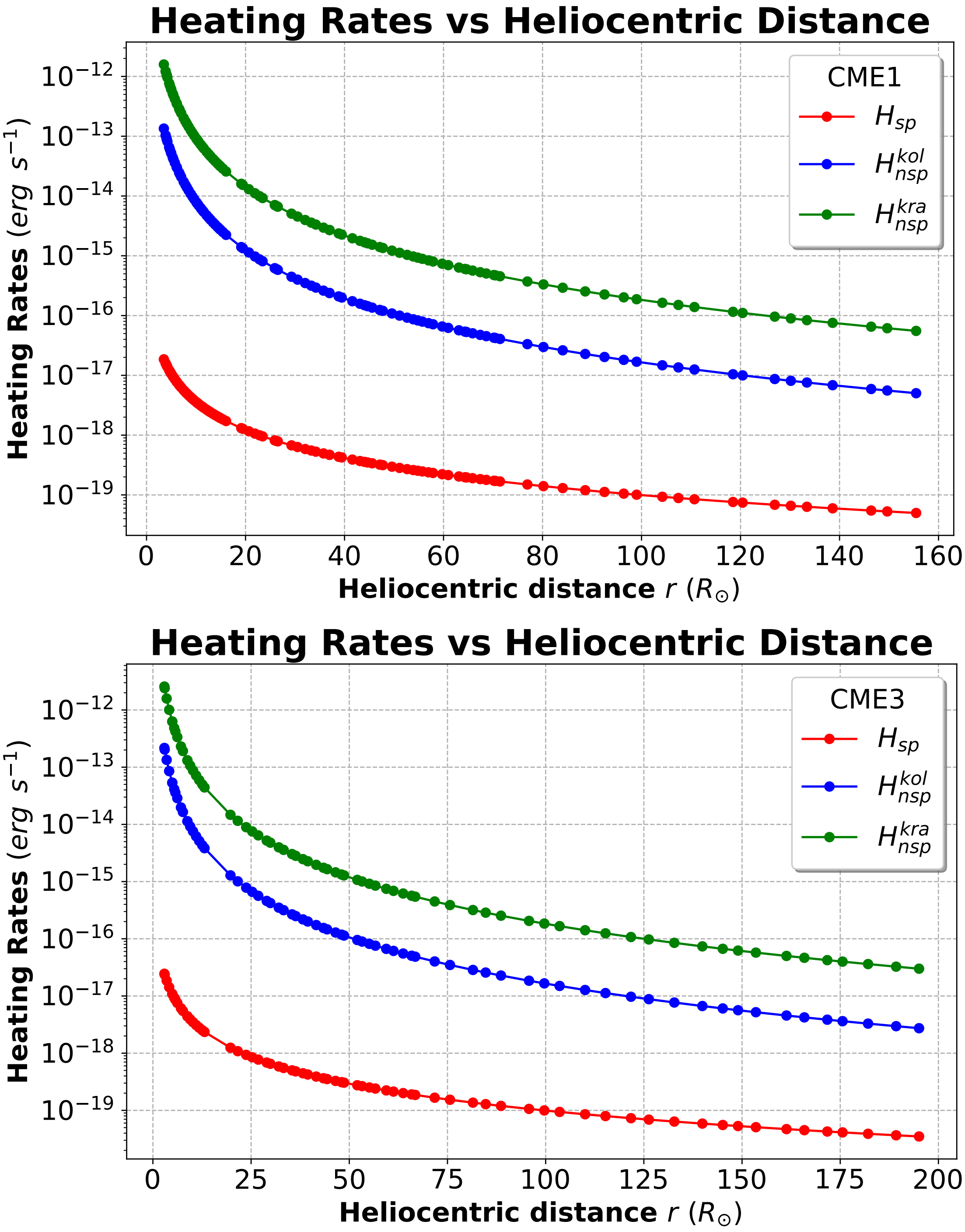

Figure 7.15: Heating Rate Profiles for CME1 & CME3

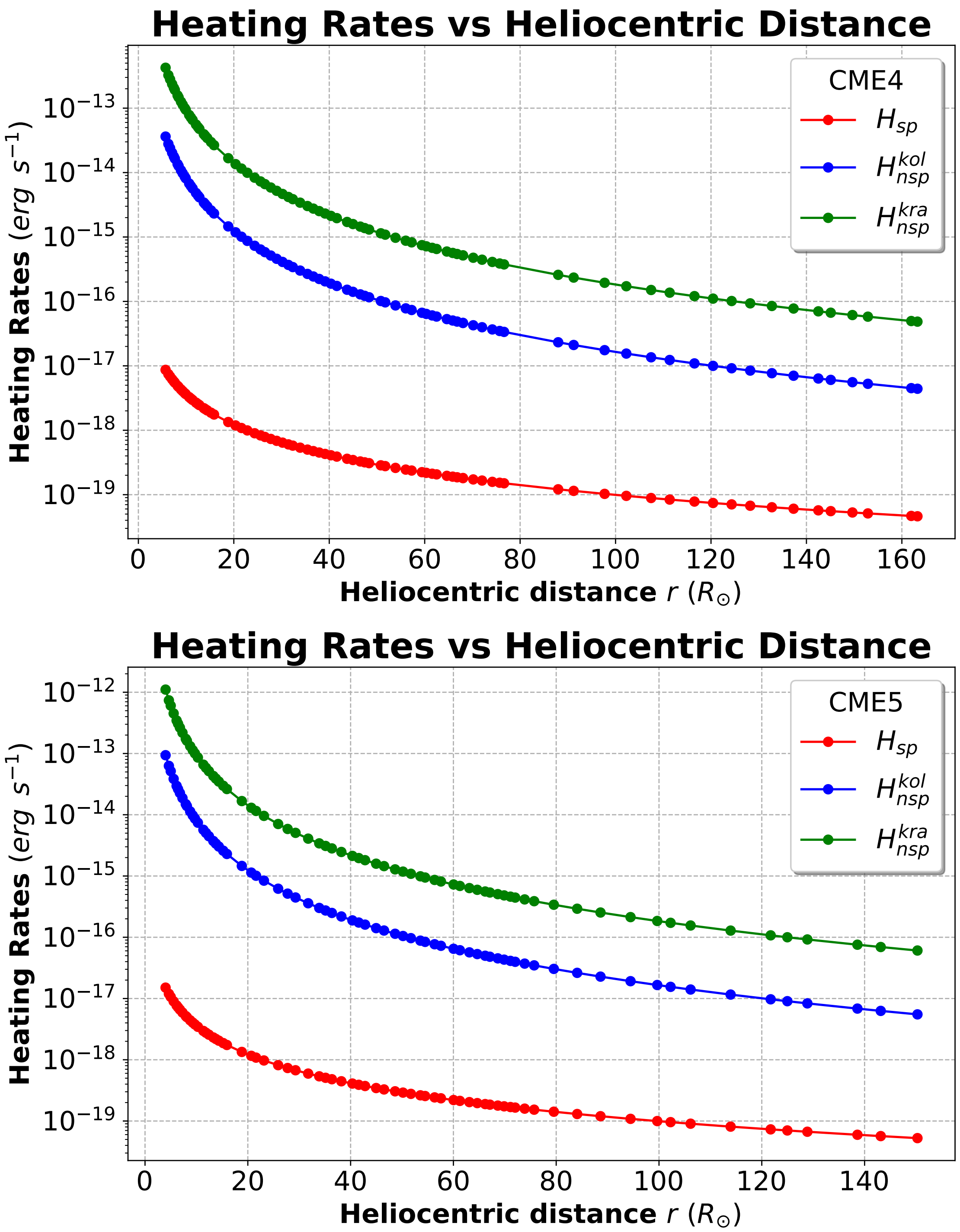

Figure 7.16: Heating Rate Profiles for CME4 & CME5

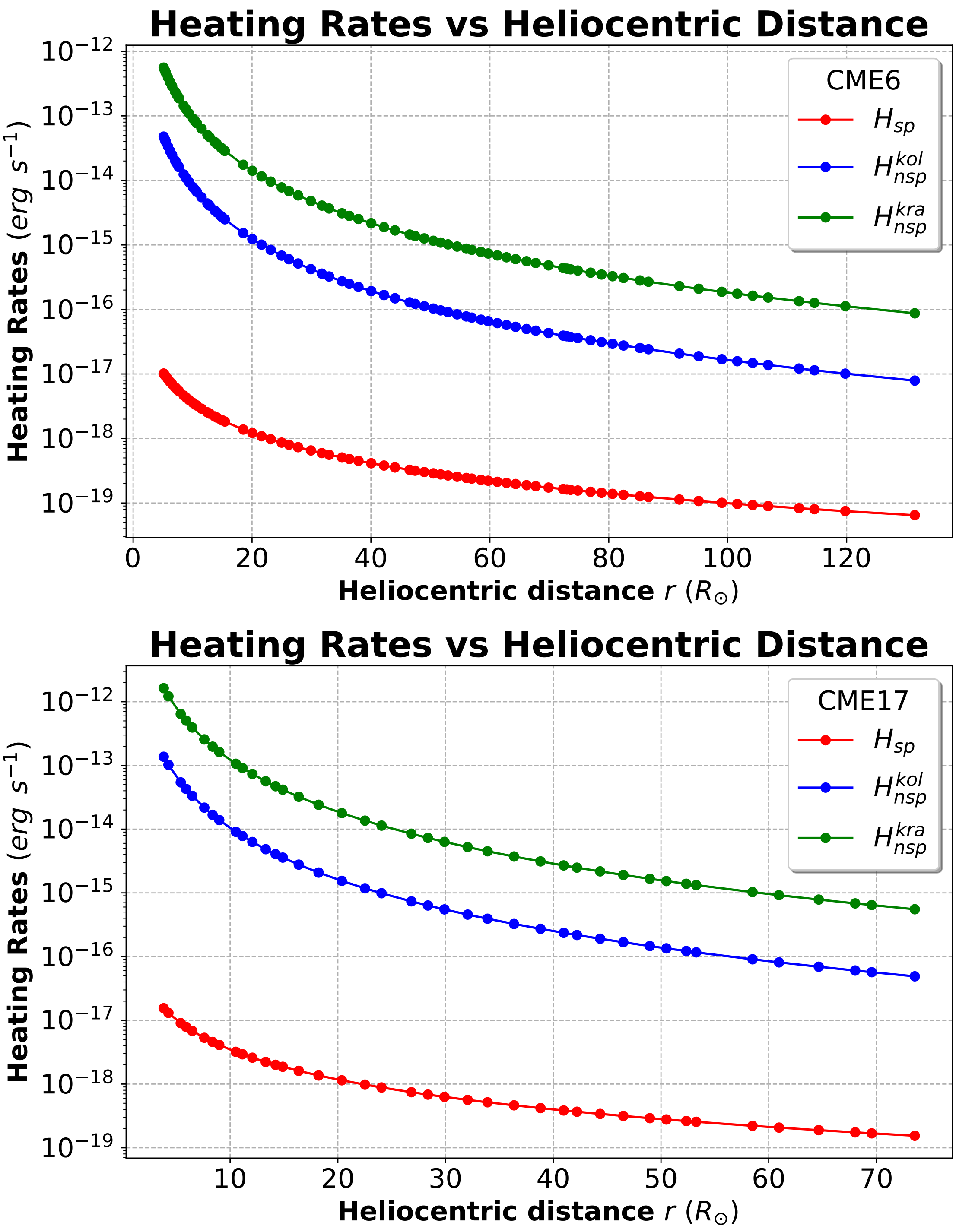

Figure 7.17: Heating Rate Profiles for CME6 & CME17

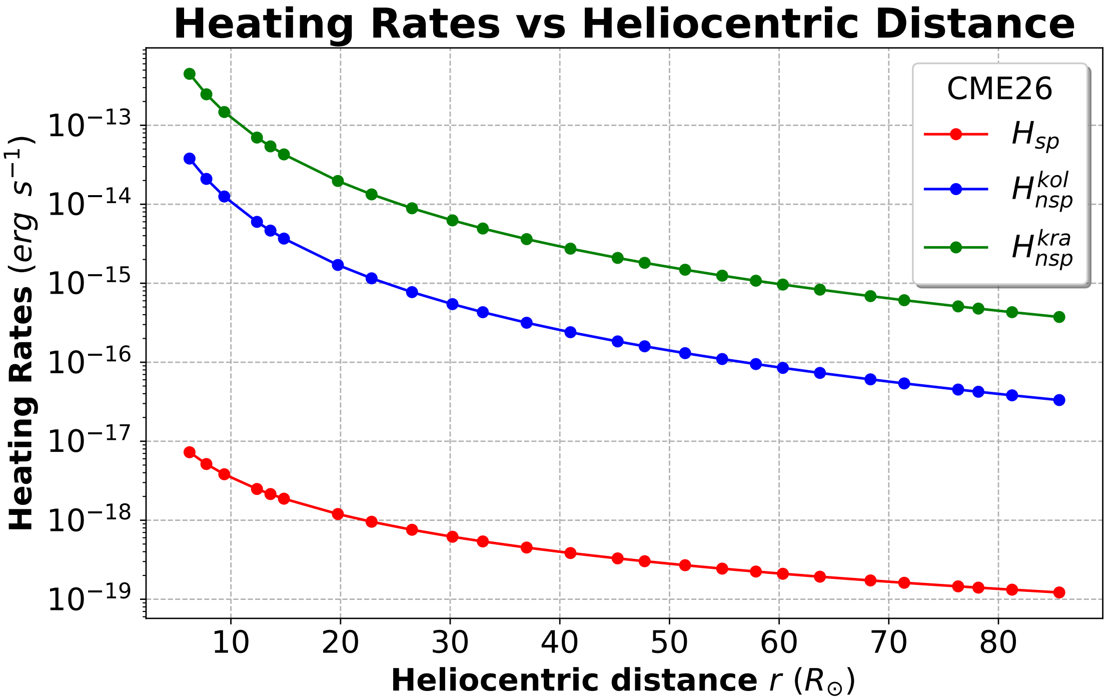

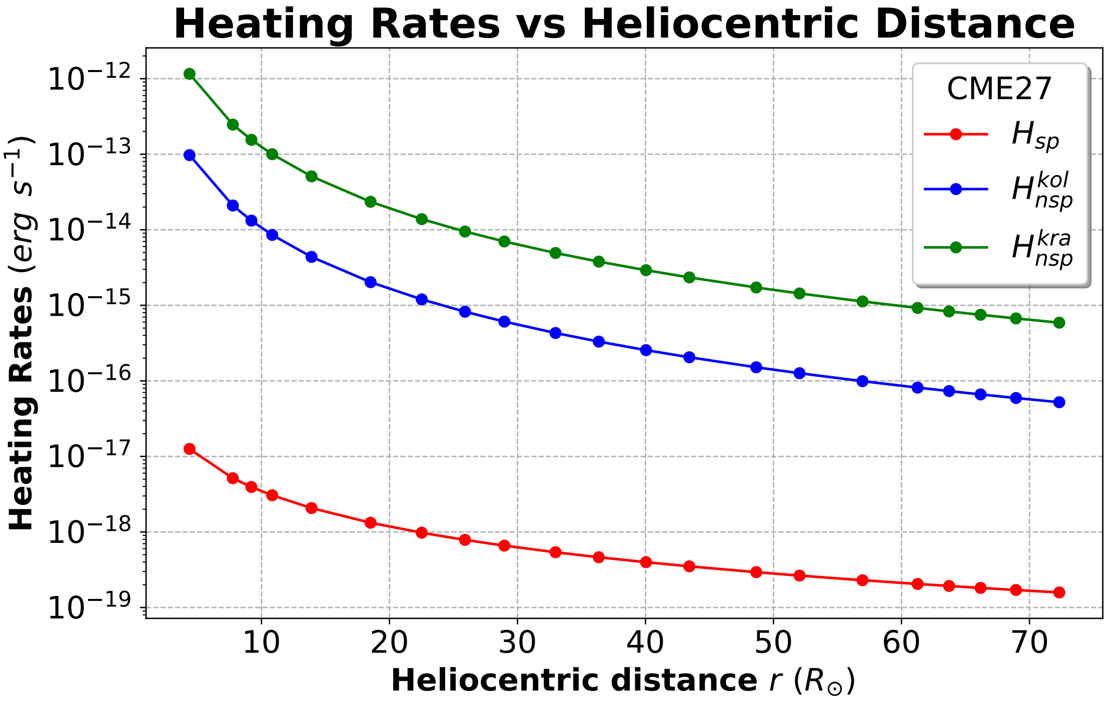

Figure 7.18: Heating Rate Profiles for CME26 & CME27

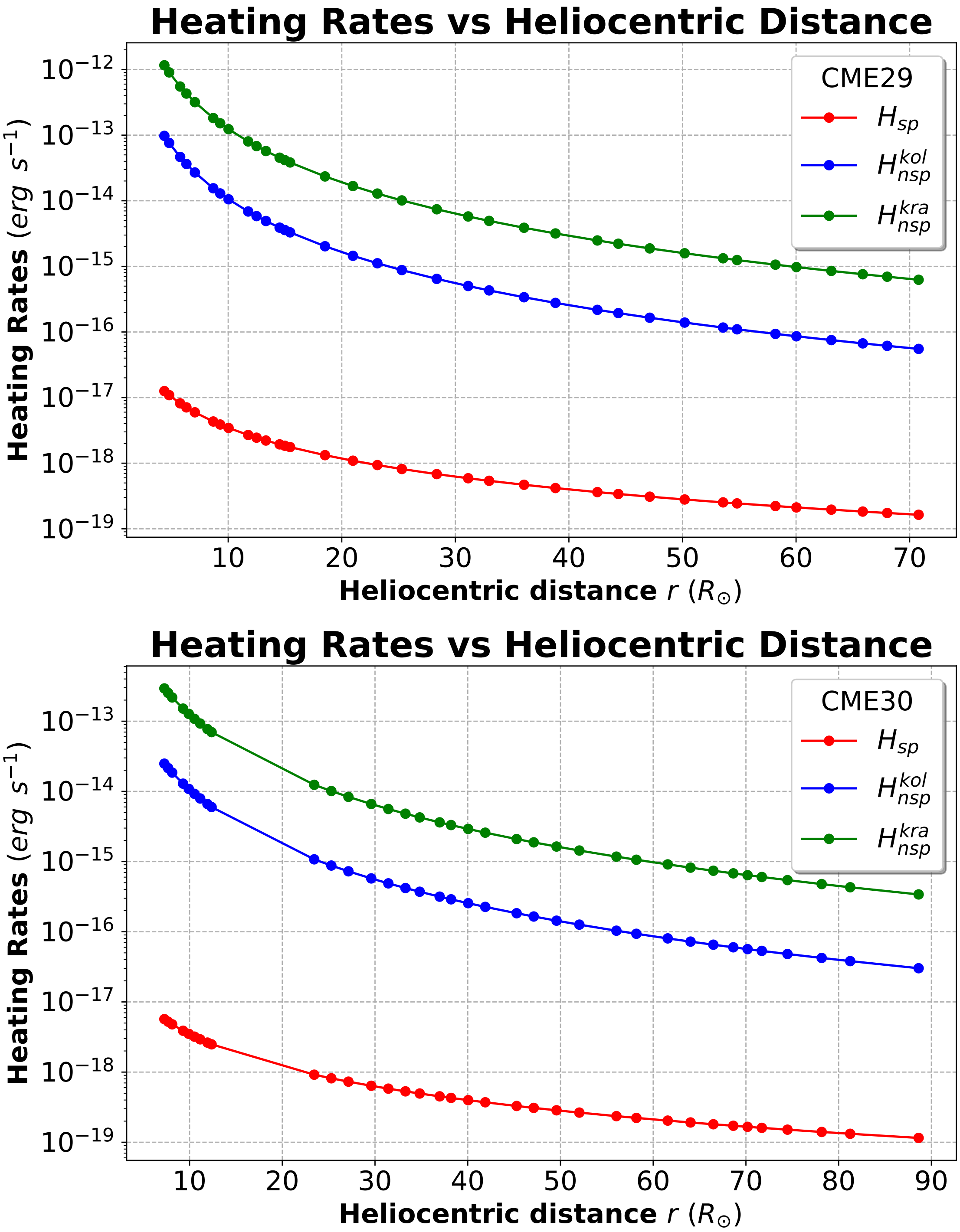

Figure 7.19: Heating Rate Profiles for CME29 & CME30

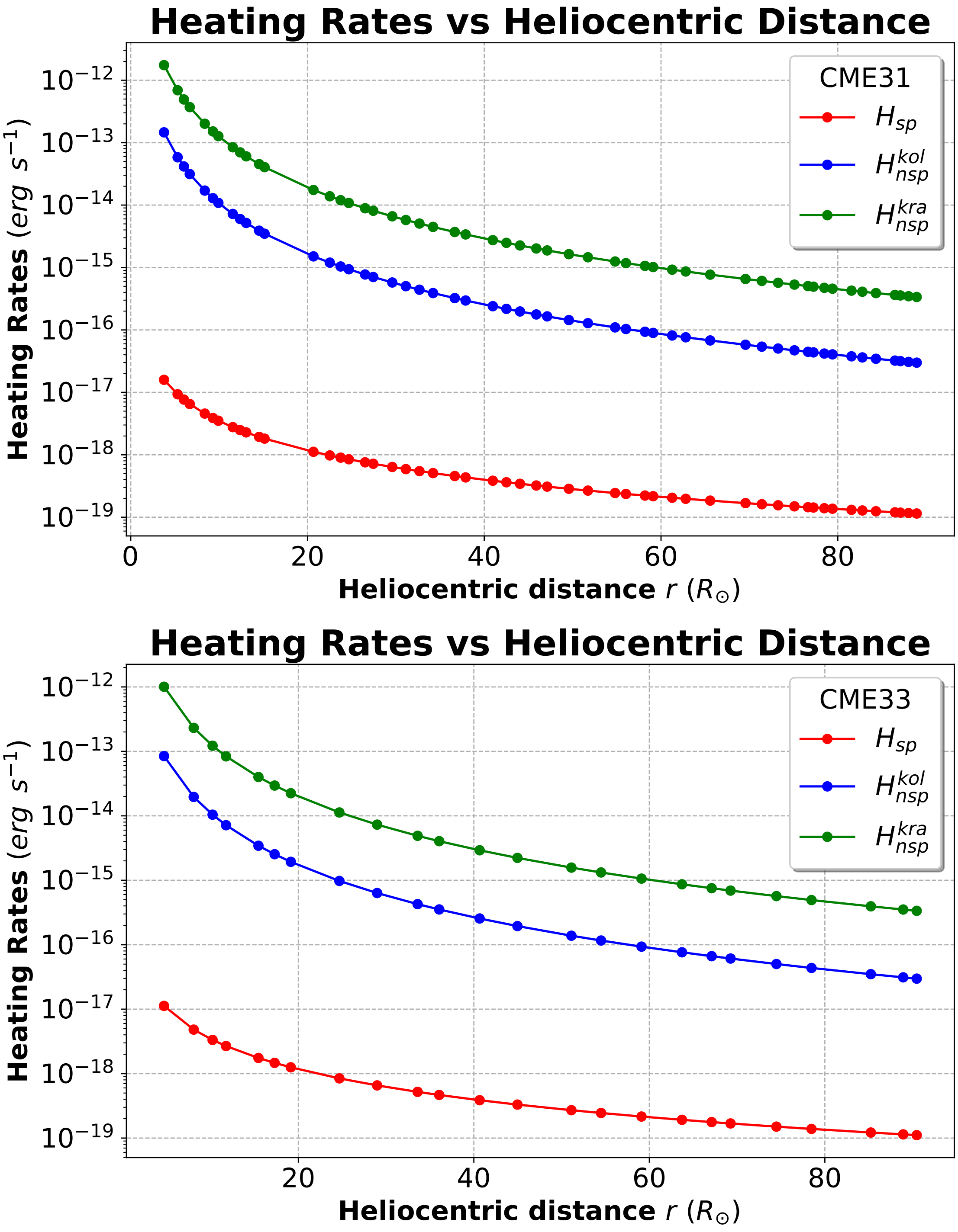

Figure 7.20: Heating Rate Profiles for CME31 & CME33

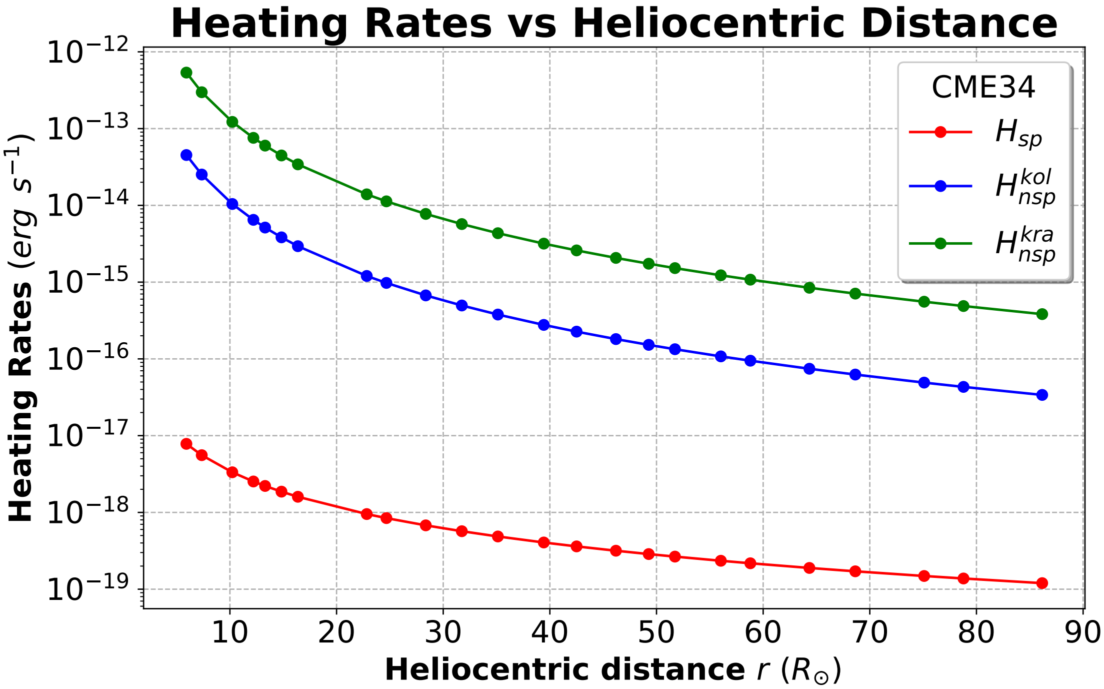

Figure 7.21: Heating Rate Profiles for CME34

Bibliography

[1] Nishtha Sachdeva, Prasad Subramanian, Angelos Vourlidas, and Volker Bothmer. CME Dynamics Using STEREO and LASCO Observations: The Relative Importance of Lorentz Forces and Solar Wind Drag. , 292(9):118, September 2017. doi: 10.1007/s11207-017-1137-9.

[2] Debesh Bhattacharjee, Prasad Subramanian, Volker Bothmer, Teresa Nieves-Chinchilla, and Angelos Vourlidas. On Modeling ICME Cross-Sections as Static MHD Columns. , 297(4):45, April 2022. doi: 10.1007/s11207-022-01982-x.

[3] Markus J. Aschwanden. *Physics of the Solar Corona. An Introduction with Problems and Solutions (2nd edition)*. 2005.

[4] S. Dasso, Pascal Demoulin, and Adriana Gulisano. Magnetic clouds along the solar cycle: Expansion and magnetic helicity. *Proceedings of the International Astronomical Union*, 7: 139–148, 07 2012. doi: 10.1017/S1743921312004759.

[5] Thomas H. Zurbuchen and Ian G. Richardson. In-Situ Solar Wind and Magnetic Field Signatures of Interplanetary Coronal Mass Ejections. , 123(1-3):31–43, March 2006. doi: 10.1007/s11214-006-9010-4.

[6] C. Möstl, M. Temmer, T. Rollett, C. J. Farrugia, Y. Liu, A. M. Veronig, M. Leitner, A. B. Galvin, and H. K. Biernat. Stereo and wind observations of a fast icme flank triggering a prolonged geomagnetic storm on 5–7 april 2010. *Geophysical Research Letters*, 37(24), 2010. doi: https://doi.org/10.1029/2010GL045175. URL `https://agupubs.onlinelibrary.wiley.com/doi/abs/10.1029/2010GL045175`.

[7] A. Thernisien. Implementation of the graduated cylindrical shell model for the three-dimensional reconstruction of coronal mass ejections. *The Astrophysical Journal Supplement Series*, 194(2):33, may 2011. doi: 10.1088/0067-0049/194/2/33. URL `https://dx.doi.org/10.1088/0067-0049/194/2/33`.

[8] Y. Wang, F. S. Wei, X. S. Feng, S. H. Zhang, P. B. Zuo, and T. R. Sun. Energetic Electrons Associated with Magnetic Reconnection in the Magnetic Cloud Boundary Layer. , 105(19): 195007, November 2010. doi: 10.1103/PhysRevLett.105.195007.

[9] N. Gopalswamy and M. R. Kundu. Estimation of the Mass of a Coronal Mass Ejection from Radio Observations. , 390:L37, May 1992. doi: 10.1086/186366.

[10] V. Yurchyshyn, S. Yashiro, V. Abramenko, H. Wang, and N. Gopalswamy. Statistical distributions of speeds of coronal mass ejections. *The Astrophysical Journal*, 619(1):599, jan 2005. doi: 10.1086/426129. URL `https://dx.doi.org/10.1086/426129`.

[11] A. Vourlidas, R. A. Howard, E. Esfandiari, S. Patsourakos, S. Yashiro, and G. Michalek. Comprehensive Analysis of Coronal Mass Ejection Mass and Energy Properties Over a Full Solar Cycle. , 722(2):1522–1538, October 2010. doi: 10.1088/0004-637X/722/2/1522.

[12] P. F. Chen. Coronal Mass Ejections: Models and Their Observational Basis. *Living Reviews in Solar Physics*, 8(1):1, April 2011. doi: 10.12942/lrsp-2011-1.

[13] R. M. E. Illing and A. J. Hundhausen. Observation of a coronal transient from 1.2 to 6 solar radii. , 90(A1):275–282, January 1985. doi: 10.1029/JA090iA01p00275.

[14] L. Burlaga, E. Sittler, F. Mariani, and R. Schwenn. Magnetic loop behind an interplanetary shock: Voyager, Helios, and IMP 8 observations. , 86(A8):6673–6684, August 1981. doi: 10.1029/JA086iA08p06673.

[15] Mahendra Verma, Dana Roberts, and Melvyn Goldstein. Turbulent heating and temperature evolution in the solar wind. *Journal of Geophysical Research*, 100:19839–19850, 10 1995. doi: 10.1029/95JA01216.

[16] Bernard J. Vasquez, Charles W. Smith, Kathleen Hamilton, Benjamin T. MacBride, and Robert J. Leamon. Evaluation of the turbulent energy cascade rates from the upper inertial range in the solar wind at 1 AU. *Journal of Geophysical Research (Space Physics)*, 112(A7): A07101, July 2007. doi: 10.1029/2007JA012305.

[17] James Chen and David A. Garren. Interplanetary magnetic clouds: Topology and driving mechanism. *Geophysical Research Letters*, 20(21):2319–2322, 1993. doi: https://doi.org/10.1029/93GL02426. URL `https://agupubs.onlinelibrary.wiley.com/doi/abs/10.1029/93GL02426`.

[18] Emilia Kilpua, Hannu E. J. Koskinen, and Tuija I. Pulkkinen. Coronal mass ejections and their sheath regions in interplanetary space. *Living Reviews in Solar Physics*, 14(1):5, November 2017. doi: 10.1007/s41116-017-0009-6.

[19] James Chen. Theory of prominence eruption and propagation: Interplanetary consequences. , 101(A12):27499–27520, December 1996. doi: 10.1029/96JA02644.

[20] V. A. Osherovich, C. J. Farrugia, L. F. Burlaga, R. P. Lepping, J. Fainberg, and R. G. Stone. Polytropic relationship in interplanetary magnetic clouds. , 98(A9):15331–15342, September 1993. doi: 10.1029/93JA01012.

[21] Ashok Kumar and D. M. Rust. Interplanetary magnetic clouds, helicity conservation, and current-core flux-ropes. , 101(A7):15667–15684, July 1996. doi: 10.1029/96JA00544.

[22] M. A. Dayeh and G. Livadiotis. Polytropic behavior in the structures of interplanetary coronal mass ejections. *The Astrophysical Journal Letters*, 941(2):L26, dec 2022. doi: 10.3847/2041-8213/aca673. URL `https://dx.doi.org/10.3847/2041-8213/aca673`.

[23] Wageesh Mishra and Yuming Wang. Modeling the Thermodynamic Evolution of Coronal Mass Ejections Using Their Kinematics. , 865(1):50, September 2018. doi: 10.3847/1538-4357/aadb9b.

[24] Georgios Nicolaou, George Livadiotis, Robert T. Wicks, Daniel Verscharen, and Bennett A. Maruca. Polytropic Behavior of Solar Wind Protons Observed by Parker Solar Probe. , 901 (1):26, September 2020. doi: 10.3847/1538-4357/abaaae.

[25] Dakeyo, Maksimovic, Démoulin, Halekas, and Stevens. Statistical Analysis of the Radial Evolution of the Solar Winds between 0.1 and 1 au, and their Semi-empirical Iso-poly Fluid Modeling. *arXiv e-prints*, art. arXiv:2207.03898, July 2022.

[26] Arnab Rai Choudhuri et al. *The physics of fluids and plasmas: an introduction for astrophysicists*. Cambridge University Press, 1998.

[27] E.R. Priest. *Solar Magnetohydrodynamics*. Geophysics and Astrophysics Monographs. Springer Netherlands, 1984. ISBN 9789027718334. URL `https://books.google.co.in/books?id=sZylLdvm7lMC`.

[28] L. Spitzer. *Physics of Fully Ionized Gases*. 1962.

[29] T. J. M. Boyd and J. J. Sanderson. *The Physics of Plasmas*. 2003.

[30] Peter Andrew Sturrock. *Plasma Physics, An Introduction to the Theory of Astrophysical, Geophysical and Laboratory Plasmas*. 1994.

[31] Debesh Bhattacharjee, Prasad Subramanian, Teresa Nieves-Chinchilla, and Angelos Vourlidas. Turbulence and anomalous resistivity inside near-Earth magnetic clouds. , 518(1):1185–1194, January 2023. doi: 10.1093/mnras/stac3186.

[32] Julián Candia and Esteban Roulet. Diffusion and drift of cosmic rays in highly turbulent magnetic fields. , 2004(10):007, October 2004. doi: 10.1088/1475-7516/2004/10/007.

[33] Andrey Nikolaevich Kolmogorov. Dissipation of Energy in Locally Isotropic Turbulence. *Akademiia Nauk SSSR Doklady*, 32:16, April 1941.

[34] Robert J. Leamon, Charles W. Smith, and Norman F. Ness. Characteristics of magnetic fluctuations within coronal mass ejections: The January 1997 event. , 25(14):2505–2508, July 1998. doi: 10.1029/98GL00305.

[35] Y. Liu, J. D. Richardson, J. W. Belcher, J. C. Kasper, and H. A. Elliott. Thermodynamic structure of collision-dominated expanding plasma: Heating of interplanetary coronal mass ejections. *Journal of Geophysical Research (Space Physics)*, 111(A1):A01102, January 2006. doi: 10.1029/2005JA011329.

[36] Robert H. Kraichnan. Inertial-Range Spectrum of Hydromagnetic Turbulence. *Physics of Fluids*, 8(7):1385–1387, July 1965. doi: 10.1063/1.1761412.

[37] Dieter Biskamp. *Nonlinear magnetohydrodynamics*. 1993.

[38] J. J. Podesta, D. A. Roberts, and M. L. Goldstein. Spectral Exponents of Kinetic and Magnetic Energy Spectra in Solar Wind Turbulence. , 664(1):543–548, July 2007. doi: 10.1086/519211.

[39] J. J. Podesta and J. E. Borovsky. Scale invariance of normalized cross-helicity throughout the inertial range of solar wind turbulence. *Physics of Plasmas*, 17(11):112905, November 2010. doi: 10.1063/1.3505092.

[40] Joseph E. Borovsky. The velocity and magnetic field fluctuations of the solar wind at 1 AU: Statistical analysis of Fourier spectra and correlations with plasma properties. *Journal of Geophysical Research (Space Physics)*, 117(A5):A05104, May 2012. doi: 10.1029/2011JA017499.

[41] C. Salem, A. Mangeney, S. D. Bale, and P. Veltri. Solar Wind Magnetohydrodynamics Turbulence: Anomalous Scaling and Role of Intermittency. , 702(1):537–553, September 2009. doi: 10.1088/0004-637X/702/1/537.

[42] D. Aaron Roberts. Evolution of the spectrum of solar wind velocity fluctuations from 0.3 to 5 AU. *Journal of Geophysical Research (Space Physics)*, 115(A12):A12101, December 2010. doi: 10.1029/2009JA015120.

[43] O. Alexandrova, C. H. K. Chen, L. Sorriso-Valvo, T. S. Horbury, and S. D. Bale. Solar Wind Turbulence and the Role of Ion Instabilities. , 178(2-4):101–139, October 2013. doi: 10.1007/s11214-013-0004-8.

[44] M. S. Venzmer and V. Bothmer. Solar-wind predictions for the Parker Solar Probe orbit. Near-Sun extrapolations derived from an empirical solar-wind model based on Helios and OMNI observations. , 611:A36, March 2018. doi: 10.1051/0004-6361/201731831.

[45] J. A. Eilek and M. Kafatos. The high-energy spectrum of hot accretion disks. , 271:804–819, August 1983. doi: 10.1086/161246.

[46] Štěpán Štverák, Pavel Trávníček, and Petr Hellinger. Electron energetics in the expanding solar wind via helios observations. *Journal of Geophysical Research: Space Physics*, 120: n/a–n/a, 10 2015. doi: 10.1002/2015JA021368.

[47] Tingyu Gou, Rui Liu, Bernhard Kliem, Yuming Wang, and Astrid M. Veronig. The birth of a coronal mass ejection. *Science Advances*, 5(3):eaau7004, 2019. doi: 10.1126/sciadv.aau7004. URL `https://www.science.org/doi/abs/10.1126/sciadv.aau7004`.

[48] X. Cheng, J. Zhang, B. Kliem, T. Török, C. Xing, Z. J. Zhou, B. Inhester, and M. D. Ding. Initiation and Early Kinematic Evolution of Solar Eruptions. , 894(2):85, May 2020. doi: 10.3847/1538-4357/ab886a.

[49] Anand D. Joshi and Nandita Srivastava. Acceleration of Coronal Mass Ejections from Three-dimensional Reconstruction of STEREO Images. , 739(1):8, September 2011. doi: 10.1088/0004-637X/739/1/8.

[50] Satabdwa Majumdar, Vaibhav Pant, Ritesh Patel, and Dipankar Banerjee. Connecting 3D Evolution of Coronal Mass Ejections to Their Source Regions. , 899(1):6, August 2020. doi: 10.3847/1538-4357/aba1f2.

[51] V. Bothmer and R. Schwenn. The structure and origin of magnetic clouds in the solar wind. *Annales Geophysicae*, 16(1):1–24, January 1998. doi: 10.1007/s00585-997-0001-x.

[52] Yuming Wang, Jie Zhang, and Chenglong Shen. An analytical model probing the internal state of coronal mass ejections based on observations of their expansions and propagations. *Journal of Geophysical Research: Space Physics*, 114(A10), 2009. doi: https://doi.org/10.1029/2009JA014360. URL `https://agupubs.onlinelibrary.wiley.com/doi/abs/10.1029/2009JA014360`.

[53] J. Martin Laming. On Collisionless Electron-Ion Temperature Equilibration in the Fast Solar Wind. , 604(2):874–883, April 2004. doi: 10.1086/382066.